

Structure-Guided Development of Deoxycytidine Kinase Inhibitors with Nanomolar Affinity and Improved Metabolic Stability

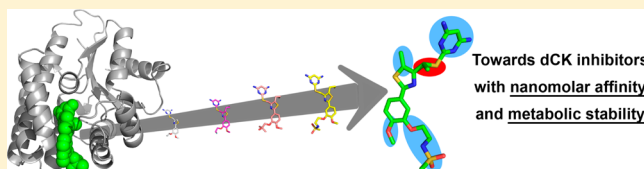
Julian Nomme,^{†,∞,#} Zheng Li,^{§,||,∞} Raymond M. Gipson,^{§,||,∞} Jue Wang,^{§,||,∞} Amanda L. Armijo,^{§,||} Thuc Le,^{§,||} Soumya Poddar,^{§,||} Tony Smith,^{§,||} Bernard D. Santarsiero,[‡] Hien-Anh Nguyen,[†] Johannes Czernin,^{§,||} Anastassia N. Alexandrova,[⊥] Michael E. Jung,[⊥] Caius G. Radu,^{*,§,||} and Arnon Lavie^{*,†}

[†]Department of Biochemistry and Molecular Genetics, and [‡]Center for Pharmaceutical Biotechnology, University of Illinois at Chicago, Chicago, Illinois 60607, United States

[§]Department of Molecular and Medical Pharmacology, ^{||}Ahmanson Translational Imaging Division, and [⊥]Department of Chemistry and Biochemistry, University of California— Los Angeles, Los Angeles, California 90095, United States

S Supporting Information

ABSTRACT: Recently, we have shown that small molecule dCK inhibitors in combination with pharmacological perturbations of de novo dNTP biosynthetic pathways could eliminate acute lymphoblastic leukemia cells in animal models. However, our previous lead compound had a short half-life in vivo. Therefore, we set out to develop dCK inhibitors with favorable pharmacokinetic properties. We delineated the sites of the inhibitor for modification, guided by crystal structures of dCK in complex with the lead compound and with derivatives. Crystal structure of the complex between dCK and the racemic mixture of our new lead compound indicated that the *R*-isomer is responsible for kinase inhibition. This was corroborated by kinetic analysis of the purified enantiomers, which showed that the *R*-isomer has >60-fold higher affinity than the *S*-isomer for dCK. This new lead compound has significantly improved metabolic stability, making it a prime candidate for dCK-inhibitor based therapies against hematological malignancies and, potentially, other cancers.



INTRODUCTION

Deoxycytidine kinase (dCK) is a deoxyribonucleoside kinase capable of phosphorylating deoxycytidine, deoxyadenosine, and deoxyguanosine to their monophosphate forms using either ATP or UTP as phosphoryl donors.¹ Phosphorylation by dCK is responsible for converting salvaged deoxycytidine into deoxycytidine monophosphate (dCMP), a precursor for both dCTP and dTTP pools. Apart from the physiological role of generating dNTPs, dCK plays a crucial role in activating multiple nucleoside analog prodrugs that are widely used in anticancer and antiviral therapy.² Recently, we^{3,4} and others⁵ identified a requirement for dCK in hematopoiesis in lymphoid and erythroid progenitors. The kinase has also been implicated in regulating the G2/M transition in response to DNA damage in cancer cells.⁶ More recently, we have shown that partial inhibition of dCK activity, combined with perturbations of nucleotide de novo synthesis pathways, was synthetically lethal to acute lymphoblastic leukemia cells but not to normal hematopoietic cells.⁷ These aspects of dCK's biology, and its potential role as a new therapeutic target in cancer, prompted us to develop small molecule inhibitors of its enzymatic activity.

In earlier publications^{8,9} we reported the discovery of hit compounds from a high throughput screen and subsequent optimization of the molecules to lead compounds **1** and **2** (numbered 36 and 37, respectively, in ref 8). Lead compounds **1**

and **2** can be divided into four distinct structural parts (Figure 1A). Part A is the pyrimidine ring, which is connected by a linker (part B) to a 5-substituted-thiazole ring (part C), which in turn is connected to a phenyl ring (part D). Conceptually, each of these parts can be modified to attain desired "druglike" properties. In previous work, we focused on the thiazole portion of the inhibitor. The crystal structure of dCK with one of the early compounds suggested that the ring 5-position could accommodate hydrophobic substituents, which led to the discovery that a propyl group at the 5-position is strongly favored over a methyl group.

To guide and rationalize the medicinal chemistry efforts in other parts of the molecule, we solved the crystal structures of human dCK with several of the inhibitors we developed. The crystal structures illuminate the relationship between the enzyme structure, the small molecule structure, and its inhibition potency. In the first part of this manuscript we report the in vitro binding affinities (IC_{50}^{app} and K_i^{app}), cellular IC_{50} values, and crystal structures of dCK in complex with compounds that differ in the pyrimidine and phenyl rings. Unfortunately, despite nanomolar affinity for dCK, when tested in a liver microsomal assay, these compounds exhibited low metabolic stability (data

Received: July 23, 2014

Published: October 23, 2014

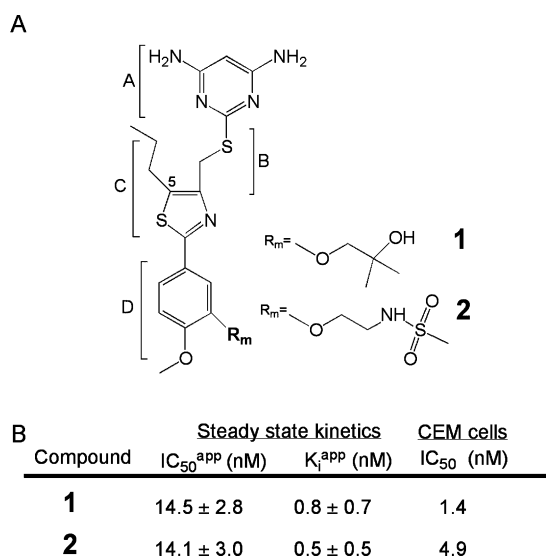


Figure 1. dCK inhibitors lead compounds. (A) Schematic representation of lead compounds **1** and **2**. These compounds are composed of four parts. Part A indicates the pyrimidine ring, and part B is the linker connecting to a 5-substituted-thiazole ring (part C), which is followed by a phenyl ring (part D). Compounds **1** and **2** differ at the substituent present at the phenyl meta position (R_m). (B) In vitro (IC₅₀^{app} and K_i^{app}) and cell (IC₅₀) properties for **1** and **2**.

not shown). This shortcoming was recapitulated by pharmacokinetic studies in mice.^{8,7}

To identify inhibitors with improved in vivo properties, we set out to explore additional chemical modifications, specifically, those that maintain the low nanomolar binding affinity of the lead compounds. In the second part of the manuscript, we report novel chiral derivatives of our inhibitors. Crystal structures of these chiral compounds bound to dCK played a key role in elucidating the chirality of the active form of the inhibitor. By combining organic chemistry intuition with detailed structural information on the target–inhibitor complex, we have identified a lead compound that retains the nanomolar affinity for dCK but has gained significant in vivo metabolic stability. This compound could play a vital role in any therapeutic strategy based on induction of DNA replication stress overload by perturbing a cancer cell's dNTP pools.

RESULTS AND DISCUSSION

The Inhibitor's Pyrimidine Ring Appears To Be Already Optimized for the Interaction with dCK. The pyrimidine ring (part A of the molecules, Figure 1A) was predicted to be the part of the molecule most difficult to improve. This is because, as observed in the crystal structures of dCK in complex with lead compounds **1** and **2** (PDB codes 4LSB and 4KCG, respectively), the inhibitor's pyrimidine ring binds to dCK at a position nearly identical to that adopted by the pyrimidine ring of the physiological substrate dC, making several hydrogen bonds, hydrophobic, and π – π stacking interactions (Supporting Information Figure S1). This binding mode suggested an already quite optimized enzyme–pyrimidine ring interaction. For compounds **1** and **2**, both pyrimidine ring exocyclic amino groups formed hydrogen-bonding interactions with side chains of Glu53, Gln97, and Asp133. Hence, not surprisingly, simultaneous removal of both amino groups resulted in complete loss of dCK inhibition.⁸ In contrast, removal of a single amino group to generate compound **3** (Figure 2A), which is identical to

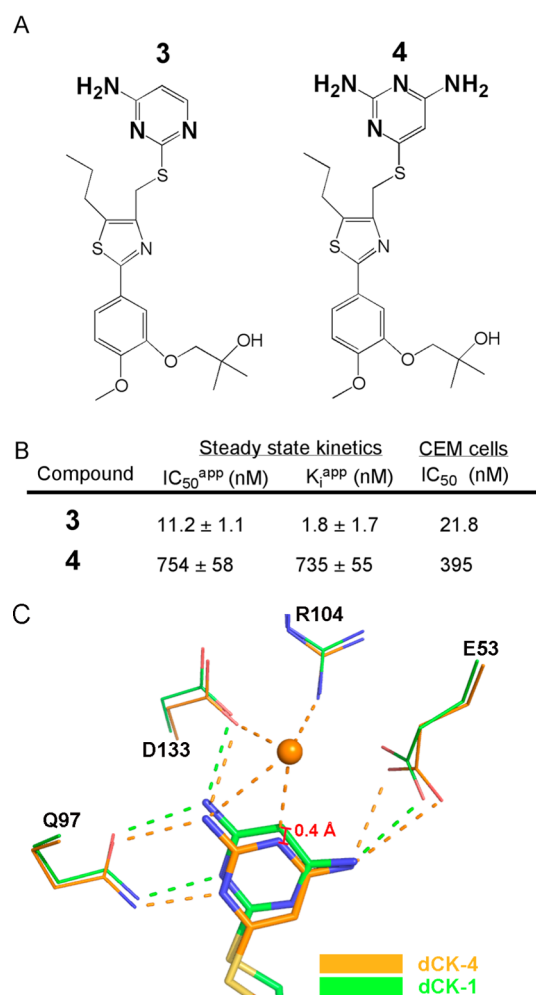


Figure 2. Modifications to the pyrimidine ring. (A) Schematic representation of compound **3** that has a single exocyclic amino group and of compound **4** that has a ring nitrogen atom between the two exocyclic amino groups. (B) In vitro (IC₅₀^{app} and K_i^{app}) and cell (IC₅₀) properties for **3** and **4**. (C) Overlay of the dCK–**4** (orange, PDB code 4Q18) and dCK–**1** (green, PDB code 4LSB) structures with a focus on the pyrimidine ring. Note the ~0.4 Å shifted position of **4** relative to **1** that is due to the presence of a water molecule (orange sphere). Binding of this water molecule is made possible by the ring N atom in compound **4**.

1 except for having a single exocyclic amino group in the pyrimidine ring (Figure 1A), resulted in similarly tight binding affinity as measured for **2** (Figures 1B and 2B). To explain how the affinity of **3** for dCK is maintained with only a single exocyclic amino group, we sought the crystal structure of the complex, but unfortunately, we were unable to obtain diffraction quality crystals. We speculate that the sole exocyclic amino group present in compound **3** is oriented in the dCK active site such that it maintains its interaction with Asp133, since only in that orientation can the neighboring pyrimidine ring N atom maintain its interaction with the side chain of Gln97 (Supporting Information Figure S1). The conclusion here is that the interaction with Glu53 made by an exocyclic amino group, when present, provides only moderate additional binding energy. While a single exocyclic pyrimidine ring amino group is sufficient for a tight interaction with dCK, in our CEM cell-based assay compound **3** exhibited a much-increased IC₅₀ value (21.8 nM, Figure 2B) relative to compound **2** (4.9 nM, Figure 1B). This

Table 1. Data Collection and Refinement Statistics

	complex											
	4	5	6	7	8	9	10	12R				
PDB code	4QI8	4QI9	4QIA	4QIB	4QIC	4QID	4QIE	4QIF				
X-ray source and detector	LS-CAT ID-G MARCCD 300	LS-CAT ID-G MARCCD 300	LS-CAT ID-G MARCCD 300	LS-CAT ID-G MARCCD 300	LS-CAT ID-G MARCCD 300	Rigaku RU-200 R-AXIS IV++	Rigaku RU-200 R-AXIS IV++	Rigaku RU-200 R-AXIS IV++				
wavelength (Å)	0.9785	0.9785	0.9785	0.9785	0.9785	1.5418	1.5418	1.5418				
temp (K)	100	100	100	100	100	93	93	93				
resolution (Å) <i>(high res in parentheses)</i>	2.0 (2.1–2.0)	2.09 (2.21–2.09)	1.90 (2.01–1.90)	2.15 (2.28–2.15)	2.0 (2.12–2.00)	2.0 (2.12–2.00)	1.85 (1.96–1.85)	2.1 (2.23–2.10)				
number of reflections												
observed	194 185	201 554	273 877	191 219	194 108	144 843	158 177	175 767				
unique	38 119	32 496	43 643	30 472	36 902	37 712	46 762	32 727				
completeness (%)	99.4 (99.9)	98.8 (93.9)	99.3 (98.4)	98.3 (97.4)	98.8 (96.1)	99.5 (98.5)	96.9 (82.8)	99.5 (98.7)				
R_{sym} (%)	5.9 (54.7)	7.3 (67.9)	4.4 (62.9)	5.2 (55.2)	5.1 (71.6)	3.3 (67.1)	2.8 (40.4)	4.3 (75.6)				
average $I/\sigma(I)$	13.6 (2.7)	14.2 (2.5)	20.64 (2.54)	17.42 (2.87)	16.57 (2.04)	19.38 (1.79)	21.62 (1.99)	21.66 (2.12)				
space group	$P4_1$	$P4_1$	$P4_1$	$P4_1$	$P4_1$	$P4_1$	$P4_1$	$P4_1$				
unit cell (Å): $a = b, c$	68.75, 122.45	68.53, 119.79	68.66, 120.36	68.97, 121.94	68.66, 119.27	68.73, 120.62	68.74, 122.20	68.78, 121.28				
refinement program	Refmac5	Refmac5	Refmac5	Refmac5	Refmac5	Refmac5	Refmac5	Refmac5				
twinning fraction	0.5	0.5	0.5	0.5	0.5	0.5	0.5	0.5				
R_{cyst} (%)	18.3	22.9	20.2	17.3	20.5	19.1	17.4	20.3				
R_{free} (%)	21.6	26.1	25.0	25.3	23.8	25.3	21.8	23.1				
resolution range (Å)	30.0–2.0	30–2.09	30–1.9	30–2.15	30–2.0	30–2.0	30–1.85	30–2.1				
protein molecules per au	2	2	2	2	2	2	2	2				
number of atoms												
protein (protA, protB)	1921, 1902	1877, 1889	1890, 1904	1877, 1873	1897, 1870	1890, 1842	1905, 1904	1897, 1897				
water molecule	88	103	105	92	109	92	185	170				
inhibitor	32 × 4	27 × 2	30 × 2	32 × 2	32 × 2	31 × 2	29 × 4	33 × 2				
UDP	25 × 2	25 × 2	25 × 2	25 × 2	25 × 2	25 × 2	25 × 2	25 × 2				
rms deviation from ideal												
bond length (Å)	0.012	0.013	0.011	0.012	0.012	0.011	0.013	0.006				
bond angles (deg)	1.66	1.84	1.65	1.70	1.72	1.68	1.67	1.03				
average B -factors (Å ²)												
protein (protA, protB)	47.0, 46.9	30.1, 30.1	40.6, 40.7	53.8, 54.6	29.5, 29.5	51.8, 51.8	37.6, 39.2	47.8, 48.7				
water molecules	39.8	29.8	39.3	45.4	29.3	46.8	38.4	44.2				
inhibitor												
protA (301, 302)	46.6, 45.8	29.9, –	39.7, –	58.7, –	29.4, –	55.8, –	43.1, 44.5	47.3, –				
protB (301, 302)	53.4, 41.2	30.0, –	40.1, –	58.3, –	29.5, –	52.8, –	40.0, 48.5	54.5, –				
UDP (protA, protB)	51.6, 49.0	30.1, 30.3	41.4, 39.9	58.4, 58.5	29.6, 29.5	53.3, 53.6	38.5, 39.4	49.8, 51.2				
Ramachandran plot (%)												
most favored regions	90.0	88.7	91.9	87.3	91.6	89.2	90.3	88.6				
additionally allowed regions	9.5	10.8	7.6	12.3	8.4	10.3	9.2	10.9				
generously allowed/disallowed regions	0.5	0.5	0.5	0.4	0.5	0.5	0.5	0.5				

result showcases the importance of evaluating the interaction between an inhibitor and its target in using both an enzymatic *in vitro* assay and a cell-based assay. Because of the reduced inhibition of dCK activity of **3** in the cell-based assay, all future compounds contained the two exocyclic amino groups.

Next, we assessed the importance of the position of the pyrimidine ring N atoms by synthesizing compound **4** (Figure 2A). This compound was measured to bind with ~50-fold higher IC_{50}^{app} relative to the very similar lead compound **1** (Figure 1A), which only differs in the position of one pyrimidine ring nitrogen atom. We solved the 2.0 Å resolution crystal structure of the dCK–**4** complex to understand how this subtle change so drastically impacted the interaction with the enzyme (see Table 1 for the data collection and refinement statistics).

All of the examined compounds bind to the open state of the enzyme, which is also the catalytically incompetent state (for a discussion about the open and closed states of dCK, see refs 10 and 11). Inhibitors bind within a deep cavity, with the pyrimidine ring of the inhibitors positioned deepest and occupying the same position occupied by the pyrimidine ring of the nucleoside substrate.^{8,9} While preventing the binding of the nucleoside substrate, our inhibitors do not interfere with binding of nucleotide to the phosphoryl donor-binding site. In fact, all crystal structures of dCK in complex with inhibitors also contained UDP at the donor site.

Despite significantly different IC_{50}^{app} values between compound **1** (14.5 nM) and compound **4** (754 nM), the pyrimidine ring of these related molecules interacts with the enzyme via very similar hydrophobic and polar interactions. The latter include Glu53, Gln97, and Asp133. However, the entire molecule **4** is displaced about 0.4 Å away from the floor of the binding cavity relative to compound **1**. (Figure 2C and Supporting Information Figure S2). The crystal structure suggests that the factor responsible for this shift is the recruitment of a water molecule (orange sphere, Figure 2C) by the pyrimidine ring N present in compound **4**. In contrast, for compound **1** the CH group in this position eliminates the potential for a hydrogen bond. This water molecule is also held in place through interactions with Arg104 and Asp133. Hence, despite formation of this additional water-mediated interaction with the enzyme, the displacement away from the enzyme caused by allowing the water molecule to bind at that position ultimately reduces the binding affinity of **4**.

On the basis of these results, we decided to maintain the original structure of the pyrimidine ring and to focus on the other parts of the molecule as potential modification sites. We next examined the effect of various substituents at different phenyl group positions (part D of the molecule, Figure 1A).

Longer Alkyl Chains with Polar Groups at the Phenyl Meta Position Increase Binding Affinity. Previously, we reported that a compound with no phenyl ring substituents, but otherwise identical to compound **1**, showed very modest potency in our CEM cell based assay ($IC_{50} = 37$ nM⁸). Adding a hydroxyl group at the meta position decreased the IC_{50} in that assay by about half (compound **5**, previously compound **31**,³ Figure 3). The effect of adding the longer hydroxyethoxy group at that position (compound **6**, previously compound **32**³) was more impressive, yielding an IC_{50} of ~1 nM (Figure 3). We are aware that primary hydroxyls as in **6** are prone to oxidation or glucuronidation,¹² but these studies do inform us as to the importance of the type of substituent at the phenyl meta position.

To understand the difference in affinities to dCK between compounds **5** and **6**, we determined the structures of dCK in complex with these molecules, solved at 2.09 and 1.9 Å

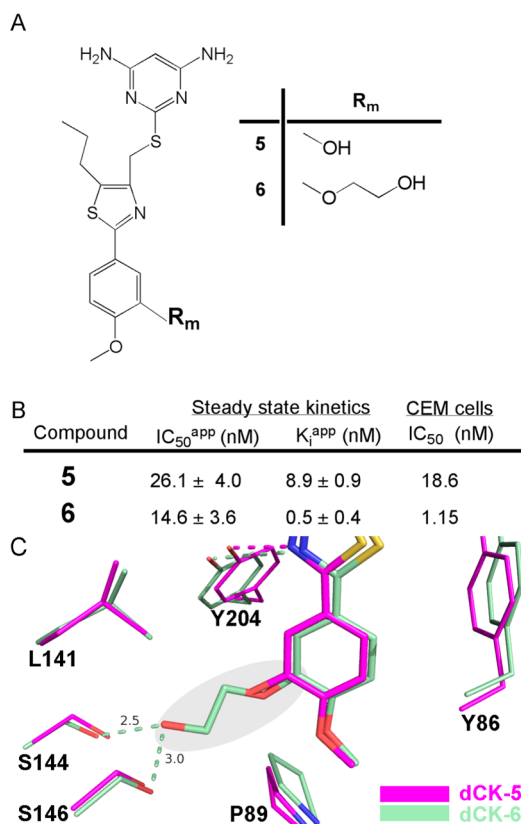


Figure 3. Modifications to the phenyl ring meta position. (A) Schematic representation of compounds **5** and **6** that differ by the nature of the meta position substituent. (B) *In vitro* (IC_{50}^{app} and K_i^{app}) and cell (IC_{50}) properties for **5** and **6**. (C) Overlay of the dCK–**5** (magenta, PDB code 4Q19) and dCK–**6** (pale green, PDB code 4Q1A) structures with a focus on the phenyl ring meta position. The tighter binding of **6** relative to **5** can be rationalized by the interaction of the longer meta substituent (position highlighted with a gray background) with S144/S146 of dCK.

resolution, respectively (Table 1). The structure of dCK in complex with compound **5** reveals that the hydroxyl group at the phenyl group meta position does not make any inhibitor–enzyme interactions. In contrast, the structure of dCK in complex with compound **6** shows that the hydroxyethoxy at this position is able to interact with the side chains of Ser144 and Ser146 (Figure 3C and Supporting Information Figure S3). We attribute this added interaction to the superior binding of compound **6** versus compound **5**.

In terms of the importance of substituents at the phenyl meta position, it is clear that having none or a short one such as a hydroxyl (compound **5**) diminishes the interaction with dCK. On the other hand, the binding affinity measured by both the *in vitro* kinetic assay and by the cell-based CEM assay of larger substituents (as present in compounds **1**, **2**, and **6**) are comparable. Previous crystal structures of dCK in complex with compound **1** (PDB code 4LSB) and **2** (PDB code 4KCG) also show an interaction between the substituent at the phenyl meta position and the enzyme, this time to Ser144. Additional side chains such as 2-fluoroethoxy poly(ethylene glycol) ($n = 2$) (PEG)₂ (**S16**, **S17**, **S19**), 2-hydroxyethyl (PEG)₂ (**S11**), 2-methoxyethyl (PEG)₂ (**S20**, **S22**, **S23**, **S25–S29**), and 2-(4,6-diaminopyrimidine-2-thio)ethyl (PEG)₂ (**S10**) substituents were well tolerated at the meta position (data not shown and Supporting Information Table S1).

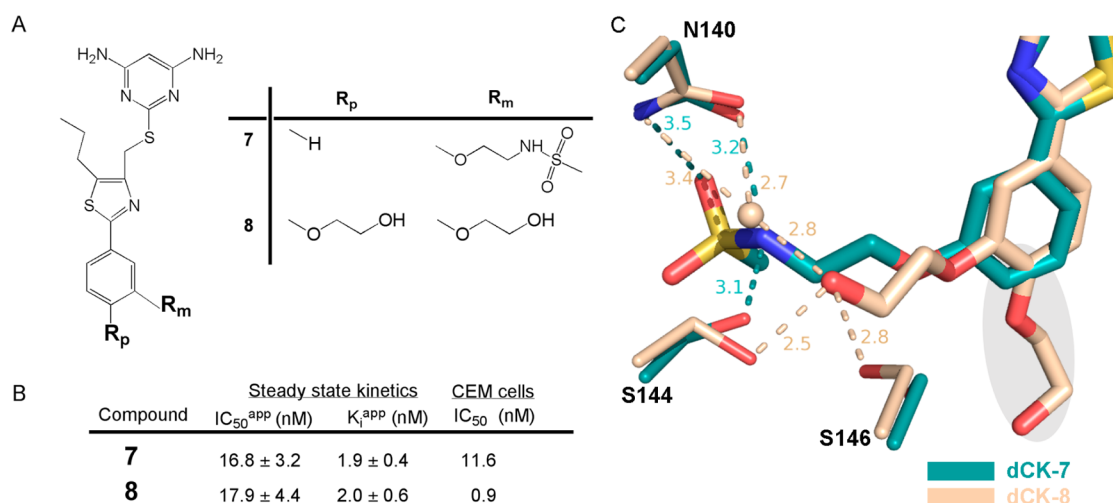


Figure 4. Modifications to the phenyl ring para position. (A) Schematic representation of compounds 7 and 8 that differ by the nature of the para position substituent. (B) In vitro (IC_{50}^{app} and K_i^{app}) and cell (IC_{50}) properties for 7 and 8. (C) Overlay of the dCK-7 (teal, PDB code 4Q1B) and dCK-8 (beige, PDB code 4Q1C) structures with a focus on the phenyl ring para position. The inhibitors bind very similarly; the meta position substituents make a direct interaction with the enzyme, but the para substituent does not. The very similar IC_{50}^{app} and K_i^{app} values of 7 and 8 are explained by the lack of direct interactions to the enzyme via the para position. In contrast, the presence of a para position substituent lowers the cell-based determined IC_{50} value.

Table 2. Human Microsomal Intrinsic Clearance Assay^a

compd	NADPH-dependent CL_{int}^a ($\mu L \min^{-1} mg^{-1}$)	NADPH-dependent $T_{1/2}$ (min)	comment
verapamil	201	11.5	high clearance control
warfarin	0.0	>240	low clearance control
1	561	4.1	
2	870	2.7	
15a (Murphy et al.)	142	16.3	
9(R/S)	419	5.5	
10(R/S)	254	9.1	
12R	22.7	102	

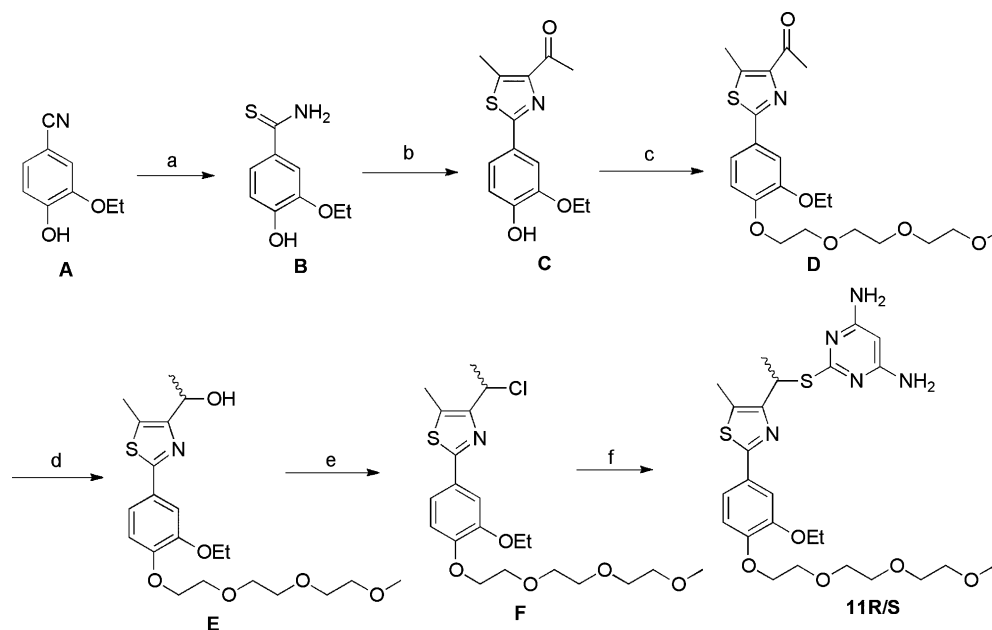
^aTest concentration of compounds was 1 μM .

We conclude that the precise nature of the substituent at the phenyl meta position is not critical as long as it contains a polar group that can extend to the proximity of Ser144/Ser146.

The Substituent at the Phenyl Group Para Position Plays a Minor Role in Binding. To determine the importance of substituent at the phenyl group para position, we prepared compound 7 (previously compound 28³), which only differs from compound 2 by lacking a para position substituent (Figure 4A). The in vitro measured binding affinity values (IC_{50}^{app} , K_i^{app}) of compound 7 are nearly identical to that of 2 (Figure 4B), indicating that substituents at the para position are not required for tight binding. This is explained by the crystal structures of dCK in complex with compounds 7 and 8 (previously compound 30³), which show a nearly identical binding mode, very similar to that observed for compound 2 (Figure 4C and Supporting Information Figure S4). The crystal structures also reveal that no significant inhibitor–enzyme interactions occur via the para substituent, if present. This conclusion is supported by the properties of compound 8, which in contrast to the methoxy group in compounds 1 and 2 has the longer hydroxyethoxy group but similar binding affinity. Hence, the in vitro binding affinities are largely unchanged between having no substituent at the phenyl group para position, having a methoxy, or the longer hydroxyethoxy. However, we did notice a ~ 10 -fold difference between compounds 7 and 8 in the CEM cell-based assay, with compound 7 being less potent. Furthermore, substituents at the

phenyl ring's para position such as 2-fluoroethoxy (S4, S14, S18), fluoro (S5, S6), methoxymethyl terminated (PEG)₂ (S21, S24), and N-substituted methanesulfonamide (S29, S30) were relatively well tolerated (data not shown and Supporting Information Table S1). Groups attached to the thiazole like 4-pyridinyl (S7), meta monosubstituted phenyl (S17), and 3,5-disubstituted phenyl ring (S31) substituents were also tolerated (data not shown and Supporting Information Table S1). Therefore, while not directly important for the binding affinity, having even a small substituent at the phenyl group para position improves the relevant cell-based measurements. As a result, most subsequent compounds contained the methoxy group at that position.

The Nature of the Thiazole Ring Substituent Dictates Metabolic Stability. In previous work we demonstrated that the nature of the substituent at the thiazole ring 5-position (part C of the molecule, Figure 1A) plays a crucial role in binding affinity.⁹ In short, we compared having no substituent at that position to having a methyl, ethyl, or propyl. We found that propyl dramatically improved the binding affinity, and as a result, compounds with a propyl at the 5-position became our lead compounds (i.e., compounds 1 and 2, Figure 1). Interestingly, compounds with a small/no substituent at the thiazole 5-position were observed to bind two inhibitor molecules per dCK active site, to binding sites that we refer to as position 1 and position 2. In contrast, the tighter binding propyl-containing molecules were

Scheme 1. Synthesis Route for Methyl Linker Compound 11(R/S)^a

^aReagents and conditions: (a) $(\text{NH}_4)_2\text{S}$ (20% in H_2O), pyridine, Et_3N , 60 °C, 85%; (b) 4-bromopentane-2,3-dione, EtOH, reflux, 95%; (c) 13-chloro-2,5,8,11-tetraoxatridecane, Cs_2CO_3 , DMF, 50 °C, 89%; (d) DIBAL-H, DCM, -78 °C, 92%; (e) SOCl_2 , DCM, 0 °C to rt; (f) 4,6-diamino-2-mercaptopyrimidine, K_2CO_3 , DMF, 75 °C, 65% in last two steps.

observed to bind with a single inhibitor molecule, at position 1, per dCK active site.⁹ This revealed that binding of two molecules is not required for high affinity. In our previous report, we analyzed the implication of single versus double binding of inhibitor molecules to dCK and concluded that inhibition of dCK is primarily caused by the binding of the inhibitor at position 1, whereas the molecule bound at position 2 does not appreciably enhance the inhibition.

However, when tested for metabolic stability, we discovered that the propyl-group-containing compounds **1** and **2** are less stable relative to those having the shorter methyl group, e.g., compound **15a** as reported by Murphy et al. (Table 2). We also explored the activity of cyclopropyl and phenyl groups at the thiazolyl 5-position (Supporting Information Table S1 and data not shown). The cyclopropyl analog (**S27**) had a good IC_{50} value, but it failed in the PET L-FAC assay.⁸ The phenyl analog (**S28**) demonstrated poor affinity. Hence we were forced to revert to the methylthiazole ring substituent despite a weaker interaction with dCK. To compensate for the loss of affinity provided by the thiazole propyl group, we searched for a compensating modification that would restore the *in vitro* binding affinity while maintaining acceptable metabolic stability. For that purpose, we decided to explore modifications on the linker moiety (part B of the compounds, Figure 1A).

Chemistry of Racemic Linker Modified Compounds.

The $-\text{SCH}_2-$ group acts to link the pyrimidine and thiazole rings of our compounds. We tested a variety of alternatives to this linker, such as its deuterated analog ($-\text{SCD}_2-$), for the purpose of a kinetic isotope study. We reasoned that if the linker was implicated in hydrolytic metabolism, then, because of the kinetic isotope effect, a deuterated ($-\text{SCD}_2-$) analog would show an improvement in metabolic stability. The deuterium analogs (**S1**, **S8**, **S9**, **S13**) had affinity similar to their isotopologues, as expected (Supporting Information Table S1 and data not shown). However, the deuterated compounds failed to show an improvement in the PET L-FAC liver assay, indicating that a

hydrolytic mechanism is probably not involved in the metabolism of the $-\text{SCH}_2-$ linker. We also tested the replacement of the sulfur atom of the $-\text{SCH}_2-$ group with a methylene group ($-\text{CH}_2\text{CH}_2-$). Replacing the sulfur atom of the linker with a carbon atom resulted in a considerable decrease in dCK affinity and metabolic stability (Supporting Information Table S1 and data not shown). We next tested a linker in which the methylene was substituted to contain a methyl group ($-\text{SCH}(\text{CH}_3)-$). These racemic methyl-linker compounds showed very promising biological results and increased metabolic stability (see Supporting Information Schemes 1 and 2 for the synthesis of compounds **9** and **10**). Therefore, we carefully examined the synthetic route in an attempt to reduce the synthetic steps and improve the total yield. We succeeded in developing a six-step synthetic route toward **11** in an overall yield of 43% (Scheme 1). Commercially available 3-hydroxy-4-methoxybenzonitrile **A** was subjected to an aqueous ammonium sulfide solution under basic conditions to provide thioamide **B**. Cyclization to form the thiazole core of **C** was achieved via condensation of thioamide **B** with 4-bromopentane-2,3-dione¹³ in refluxing ethanol. Introduction of a PEG chain into the phenyl ring of compound **D** with 13-chloro-2,5,8,11-tetraoxatridecane¹⁴ under basic conditions was achieved in 89% yield. Reduction of the resulting ketone-containing compound with diisobutylaluminum hydride (DIBAL-H) afforded racemic secondary alcohol **E** in high yield. Alcohol **E** was converted to the respective chloride **F** with thionyl chloride. The acyl chloride was reacted in crude form with 4,6-diamino-2-mercaptopyrimidine to generate product **11R/S**.

The Chirality of the Linker Methyl Group Is a Critically Important Determinant of Binding Affinity. The $-\text{SCH}(\text{CH}_3)-$ linker was introduced to a compound that contained the propyl group at the thiazole ring 5-position (compound **9**) and to a compound that, instead of the propyl group, contained a methyl (compound **10**) (Figure 5A). As mentioned above, the rationale for compound **10** was the predicted improvement in

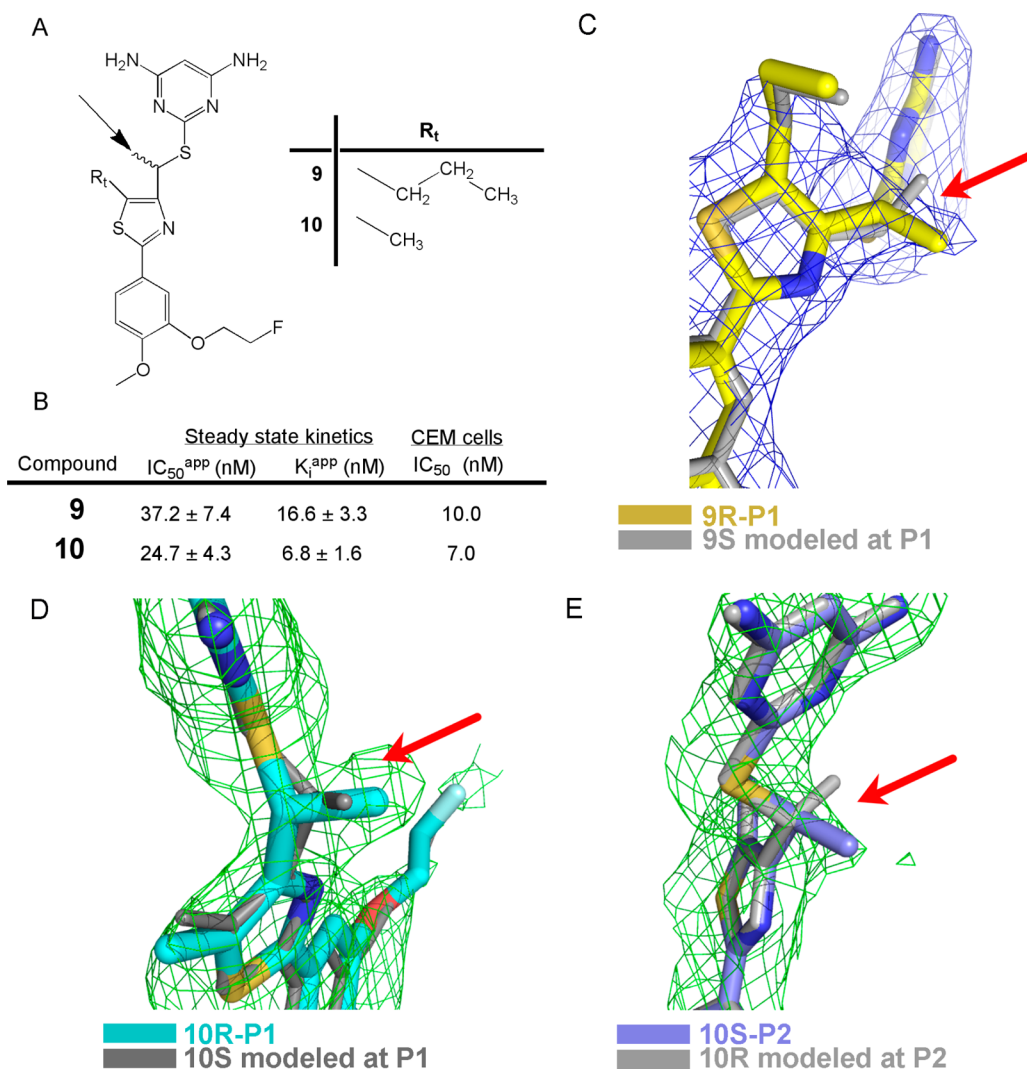


Figure 5. Modifications to the linker. (A) Schematic representation of compounds **9** and **10**. Both compounds were synthesized as the racemic mixture (*R/S*); the addition of a methyl group (arrow) to the methylene linker group makes these compounds chiral. Whereas **9** has a propyl group at the thiazole ring 5-position (R_t), **10** has a methyl group. (B) In vitro (IC_{50}^{app} and K_i^{app}) and cell (IC_{50}) properties for **9** and **10**. (C) The propyl group at the thiazole ring makes **9** bind as a single molecule to binding site position 1 of dCK (see text for details). Notably, despite forming the enzyme–inhibitor with racemic **9**, in the crystal structure we observe only the *R*-isomer (compound **9** in yellow, PDB code 4Q1D; $F_o - F_c$ omit map in blue contoured at 2σ). A theoretical model of the *S*-isomer (gray) demonstrates that only the *R*-isomer fits the electron density. (D) The methyl group at the thiazole ring permits two molecules of **10** to bind to dCK: one to position 1 and one to position 2. In position 1 we observe only the *R*-isomer (10R-P1, cyan, PDB code 4Q1E; $F_o - F_c$ omit map contoured at 2σ in green). A theoretical model of the *S*-isomer at position 1 (gray) clearly demonstrates that only the *R*-isomer fits the electron density (red arrow). (E) In position 2 we observe only the *S*-isomer (10S-P2, plum, PDB code 4Q1E; $F_o - F_c$ omit map contoured at 1.5σ in green). A theoretical model of the *R*-isomer at position 2 (gray) clearly demonstrates that only the *S*-isomer fits the electron density (red arrow).

metabolic stability. Interestingly, whereas compounds with a propylthiazole ring previously showed tighter binding to dCK compared to the analogous methylthiazole compounds, we now measured better binding with the methyl-containing compound **10** to the propyl-containing compound **9** (Figure 5B). Hence, the proximity of the thiazole-ring substituent (propyl or methyl) to the methyl-linker substituent resulted in the larger propyl group being not as accommodating in the dCK active site. Despite the improved in vitro binding parameters for **10** over **9**, the cell-based assay yielded similar IC_{50} values, yet consistent with **10** being superior (Figure 5B).

Both compounds **9** and **10** were prepared as racemic mixtures; the introduced linker-methyl group makes that position a new chiral center (arrow, Figure 5A). To elucidate which of the two enantiomers is the active dCK inhibitor, we determined the

crystal structure of dCK in complex with compounds **9** and **10** (solved at 2.0 and 1.85 Å resolution, respectively, Table 1). As expected, compound **9** binds as a single molecule to dCK, specifically at position 1, because of the presence of the propyl group in the thiazole ring. Interestingly, despite the fact that a racemic mixture of **9** was used to form the complex to dCK, the crystal structure provides unambiguous evidence for the *R*-isomer binding at position 1 (Figure 5C and Supporting Information Figure S5). Likewise, inspection of the structure of the complex between racemic **10** and dCK shows that the *R*-isomer occupies the most relevant position 1 binding site (Figure 5D and Supporting Information Figure S5). Since compound **10** contains the methyl substituent in the thiazole ring, which allows for a molecule to also occupy position 2, we observe compound **10** at that position as well. However, whereas it is the *R*-isomer of

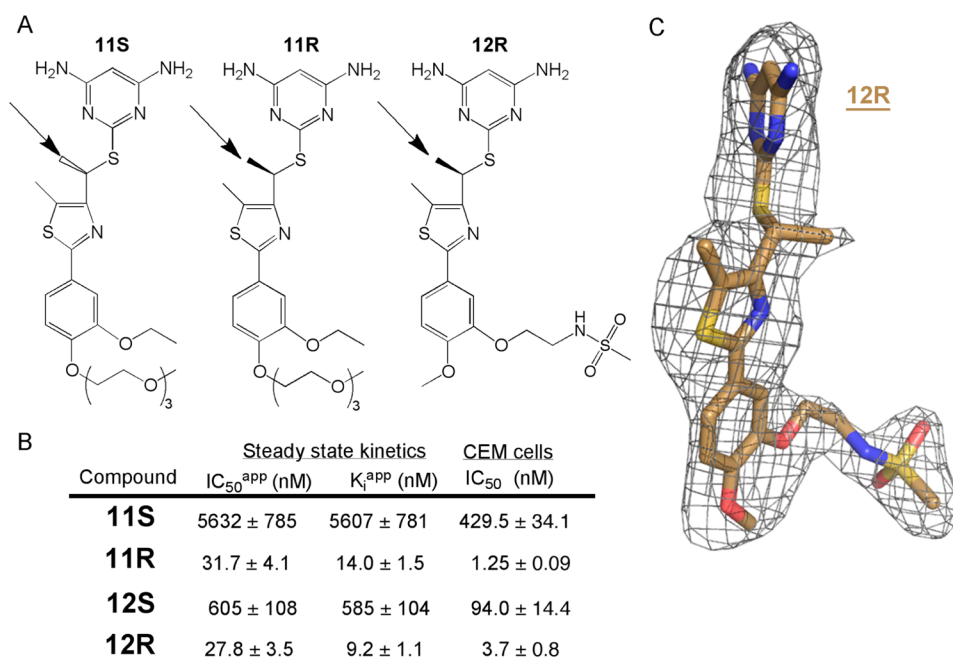


Figure 6. The *R*-isomer is the relevant isomer regarding dCK inhibition. (A) Schematic representation of compounds 11S, 11R, and 12R (*R* or *S* designate the chirality of the linker methylene carbon; arrows point at the added methyl group). (B) In vitro (IC_{50}^{app} and K_i^{app}) and cell (IC_{50}) properties for 11S, 11R, and 12R. The *R*-isomer of both 11 and 12 is responsible for the observed inhibition of the enzyme. (C) dCK was crystallized in the presence of enantiomerically pure 12R, and the enzyme–inhibitor complex structure was solved (PDB code 4QJF). $F_o - F_c$ omit map (1.6σ) for the position 1 binding site clearly shows the presence of 12R (brown). Despite the thiazole methyl group in 12R (which is compatible with molecules also binding to position 2), we do not observe a second 12R molecule at position 2. This is consistent with the results with compound 10 (Figure 5) that showed that only the *S*-isomer binds to position 2.

10 that binds to position 1, it is the *S*-isomer that binds to position 2 (Figure 5E and Supporting Information Figure S5).

We previously concluded that position 1 is the critical binding site for this family of inhibitors. This would suggest that the measured in vitro inhibition values of racemic 10 are reflecting the preferential binding of the *R*-isomer. To test this, we synthesized compound 11, which is a slight modification of 10 (the nature of the phenyl group substituents) but notably had the racemic mixture separated to yield the pure isomers 11R and 11S (Figure 6A). We determined the in vitro binding affinities of the enantiomerically pure compounds and observed that 11S has ~400-fold weaker binding affinity relative to 11R (Figure 6B). This result provides clear evidence that the *R*-form is responsible for the tight interaction with dCK. This result also validates our structure-based interpretation that position 1 is the one most relevant inhibitor binding site for dCK inhibition and that position 2 is occupied because of the high concentration of the inhibitor used in the crystallization setups.

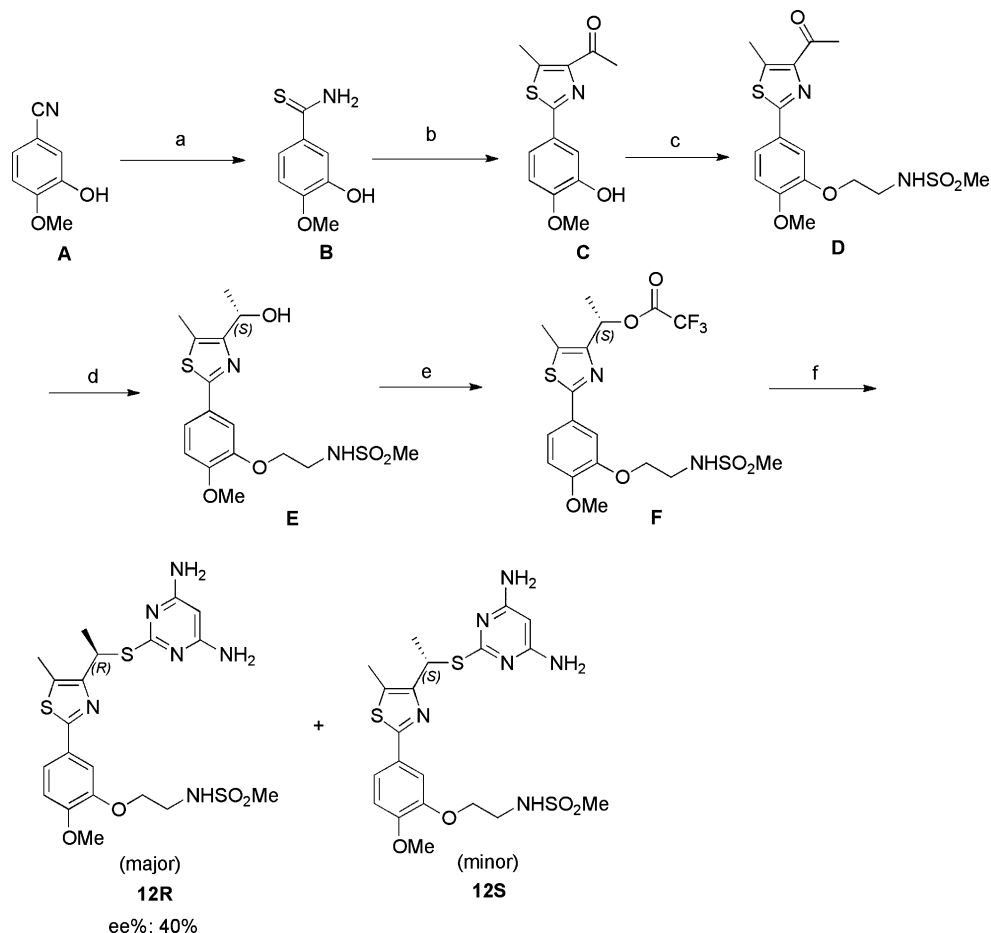
Enantioselective Synthesis of Chiral Molecules. Having discovered that the *R*-isomers of compounds 9, 10, and 11 are responsible for the dCK inhibition, we set out to develop an asymmetric synthesis (Scheme 2). The chiral synthesis developed by our group for compound 12R, which is a close analog of 10, features a chiral Corey–Bakshi–Shibata (CBS) reaction¹⁵ of ketone D. Chiral alcohol E was synthesized according to this method with an enantiomeric excess of 96%, as determined via chiral HPLC. Employing mesic or tosic anhydride to give the sulfonates under different basic conditions such as Et_3N , pyridine, or DMAP resulted in elimination to the alkene, presumably due to the stability of the secondary benzylic-like carbocation. The use of trifluoroacetic anhydride (TFAA) at 0 °C converted alcohol E into the corresponding trifluoroacetate (TFA) F without a significant decrease in the % ee of the ester.

Finally, compound F was reacted with 4,6-diamino-2-mercapto-pyrimidine to generate 12R in 61% yield over two steps with an enantiomeric excess of 40%. Presumably, a portion of the reaction occurs via a direct S_N2 pathway, while another part occurs via an S_N1 pathway, and thereby racemized material was obtained. Chiral resolution via recrystallization generated 12R with an enantiomeric excess of over 90%. Likewise, (*S*)-(-)-2-methyl-CBS-oxazaborolidine was used in the CBS reduction to synthesize 12S.

Characterization of Enantiomerically Pure 12R. Compound 12R (Figure 6A) was measured to have very similar in vitro binding affinities to 11R (Figure 6B). Significantly, just as the affinity of 11S was much reduced relative to 11R, the affinity to dCK of 12S was much reduced relative to 12R. This reiterated the preference of dCK for compounds that contain the *R*-isomer of the linker.

We solved the dCK–12R complex crystal structure. We expected 12R to bind only at position 1 based on the previous structure with compound 10 (observing 10R bound at position 1) and the kinetic results using enantiomerically pure 11S, 11R, 12S, and 12R (observing higher affinities for the *R*-isomers) and since the crystals were formed with the enantiomerically pure 12R. Additionally, lacking the *S*-isomer, we expected a vacant position 2 binding site. Indeed, the crystal structure of the dCK–12R complex revealed a single inhibitor molecule at position 1 (Figure 6C). This result suggests that the *R*-isomer has very low affinity to the binding site at position 2. Notably, while the interaction between the *R*-isomer and dCK is limited to the position 1 binding site, this does not diminish the binding affinity for the enzyme.

Determinant of Chiral Selectivity. What could be behind the dramatic selectivity of the dCK position 1 binding site for the *R*-isomers of the inhibitors? Likewise, what prevents the *R*-

Scheme 2. Asymmetric Synthesis Route of 12R^a

^aReagents and conditions: (a) $(\text{NH}_4)_2\text{S}$ (20% in H_2O), pyridine, Et_3N , 60 °C, 85%; (b) 4-bromopentane-2,3-dione, EtOH , reflux, 96%; (c) *N*-(2-bromoethyl)methanesulfonamide, Cs_2CO_3 , DMF, 50 °C, 82%; (d) (*R*)-(+)-2-methyl-CBS-oxazaborolidine, BH_3 -THF complex, THF, -78 °C, 77%, (96% ee); (e) TFAA, DCM, 0 °C, (f) 4,6-diamino-2-mercaptopyrimidine, DMF, 80 °C, 61% in last two steps.

isomer from binding at position 2, while this binding site is compatible with the binding of the *S*-isomer? The simple explanation would involve steric considerations relating the inhibitor and enzyme, where the chiral methyl group of the linker clashes with enzyme residues in the case of one isomer but not the other. However, inspection of the crystal structures solved with compounds **10(R/S)** and **12R** does not support this interpretation; we could model the *S*-isomer bound to position 1 (Figure 5D) and the *R*-isomer bound at position 2 (Figure 5E) with no apparent clashes.

Comparison of the binding mode between **10R** and **10S** reveals that the relative orientation of the pyrimidine ring to the thiazolephenyl part is strikingly different between the *R* and *S* isomers (Figure 7A and Figure 7B). That is, by a change of the angles of the linker that connects the pyrimidine ring to the thiazole ring, each isomer has adjusted its conformation to best fit its binding site (i.e., induced fit). This demonstrates that the enzyme dictates the relative orientations between the pyrimidine ring, linker, and the thiazolephenyl rings. It also shows that the relative orientation between thiazole and phenyl rings (being coplanar) is largely unchanged, not surprising because of the resonance between the rings.

To further probe the observed chiral selectivity, we constructed a theoretical model of **10S** binding at position 1 with the same orientation as **10R**. Whereas the observed distance

between the chiral methyl of the linker and the thiazole ring methyl group for **10R** in position 1 is 4.2 Å (Figure 7C), for the modeled **10S** bound to position 1, that distance would be an unfavorable 2.5 Å (Figure 7D). Likewise, whereas the observed distance between the chiral methyl and the thiazole methyl for **10S** in position 2 is 4.4 Å (Figure 7E), for the modeled *R*-isomer adopting the same conformation as **10S**, that distance would be an unfavorable 2.6 Å (Figure 7F). Hence, the strict chiral selection to either position 1 or position 2 is due to the enzyme dictating a particular inhibitor orientation that is vastly different between the binding sites. In the case of position 1, that orientation is not compatible with the *S*-isomer, and for position 2, that orientation is not compatible with the *R*-isomer.

Using computer simulations, we obtained a qualitative estimate of the conformational penalty incurred by **10R** and **10S** upon binding with the protein. The conformational penalty is the energy difference between the preferred solution-phase geometry of a substrate and the geometry that it assumes upon binding: $\Delta E = E_{\text{solution}} - E_{\text{bound}}$. Each enantiomer was docked with the solvated protein at position 1 and allowed to equilibrate (see details in Experimental Section and Supporting Information Figure S6). The equilibrated, docked inhibitor structures were removed from the protein, and their energies were assessed with the semiempirical PDDG/PM3 method.^{16–21} Unbound structures of **10R** and **10S** were optimized in implicit solvent to

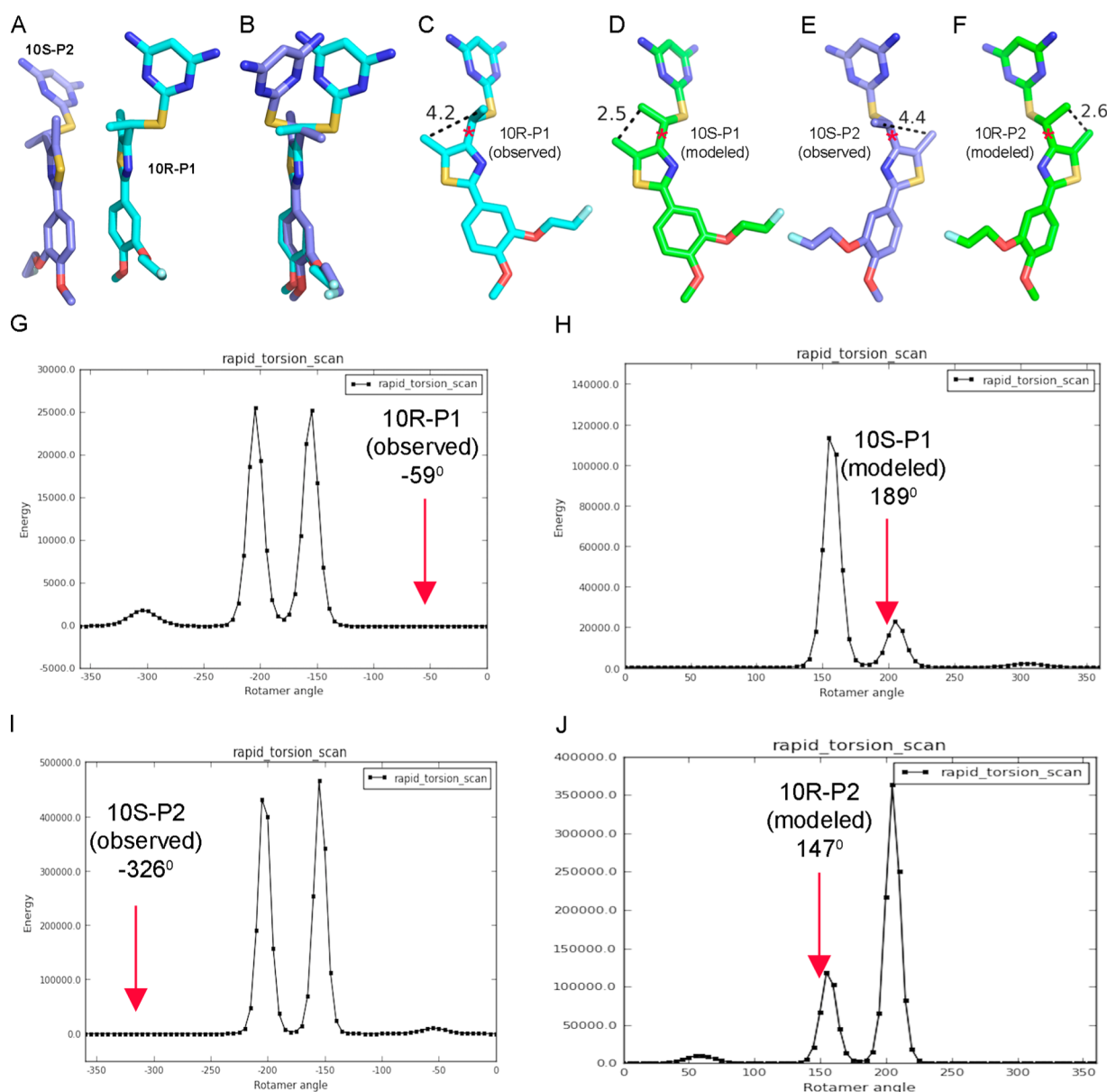


Figure 7. Chiral selectivity is due to conformational selection by the enzyme's binding site. (A) Observed orientation of **10R** (cyan) at position 1 (10R-P1, PDB code 4Q1E) and **10S** (plum) at position 2 (10S-P2) upon dCK binding. (B) **10S** overlaid on **10R** based on the thiazole ring. Note the different relative orientations of the thiazole and pyrimidine rings between **10R** and **10S**. (C) The conformation of **10R** (10R-P1) is dictated by the position 1 binding site. In this conformation the distance between the chiral linker methyl group and the thiazole ring methyl group is 4.2 Å. (D) The theoretical model of **10S** binding with the same conformation as **10R** in position 1 (10S-P1) shows that the homologous distance is reduced to 2.5 Å. (E) The conformation of **10S** (10S-P2) is dictated by the position 2 binding site. In this conformation the distance between the chiral linker methyl group and the thiazole ring methyl group is 4.4 Å. (F) The theoretical model of **10R** binding with the same conformation as **10S** in position 2 (10R-P2) shows that the homologous distance is reduced to 2.6 Å. (G) For 10R-P1, the observed torsion angle between the thiazole ring and the linker is -59° . Scanning possible torsion angles shows that this value represents a low energy conformation of **10R**. (H) For 10S-P1, the observed torsion angle is 189° . This value corresponds to a high-energy conformation of **10S**. (I) For 10S-P2, the observed torsion angle is -326° . Scanning possible torsion angles shows that this value is at a low energy conformation of **10S**. (J) For 10R-P2, the observed torsion angle is 147° . This value corresponds to a high-energy conformation.

determine their low-energy solution-phase conformations. As with the bound structures, energies of the unbound structures were assessed with PDDG/PM3. The resulting energies were used to obtain qualitative conformational penalties for each enantiomer. The conformational penalty for **10S** was almost twice the conformational penalty for **10R** (45 kcal/mol larger penalty for **10S**), further demonstrating that **10R** needs to undergo a much less unfavorable structural rearrangement in order to bind with the protein at position 1.

Another way of considering this issue is to examine the energy of the inhibitor as a function of rotation around the bond that connects the thiazole ring to the chiral linker atom (bond marked with * in Figure 7C–F). For **10R** bound to dCK at position 1, the observed dihedral angle that specifies this rotation is -59° and fits a low energy conformation (Figure 7G). In contrast, the modeled S-isomer at this binding site would have a torsion angle of 189° , which is clearly a high-energy conformation (Figure 7H). The same pattern is observed for position 2, with the S-isomer binding to dCK with a torsion angle of -326° , which is a

low energy conformation, while the modeled *R*-isomer at that position is a high-energy conformation (Figure 7I and Figure 7J). Hence, the chiral selectivity does not come directly from the enzyme sterically favoring one isomer over the other. Rather, the enzyme dictates a particular conformation, and the selectivity comes from one isomer being able to adopt that particular conformation, whereas the energy penalty for the other isomer precludes its binding.

In addition to explaining the chiral selectivity for the compounds discussed here, this understanding can be used for the design of chiral molecules that bind to either binding site. Specifically, the prediction would be that replacing the thiazole methyl group with a hydrogen atom would eliminate any steric clash to the chiral methyl group, and hence either isomer could bind to either inhibitor binding site.

Improved Metabolic Stability of 12R. We first determined the metabolic stability of **12R** in a standard microsomal liver clearance assay. The NADPH-dependent $T_{1/2}$ of **12R** was ~37-fold longer than that of our previous lead compound **2** (Table 2). We then tested compound **12** in mice, using our previously described positron emission tomography (PET) assay.⁸ Whereas our earlier lead compound **2** retained only ~25% inhibition of dCK activity 4 h after dosing by intraperitoneal injection,³ compound **12** (given as the racemic mixture) exhibited >50% inhibition of dCK activity at this time point (Figure 8A). Furthermore, 8 h after treatment with compound **12**, dCK inhibition was still above 30%. We then determined the pharmacokinetic properties of compound **12** to compare with our previous lead compounds **1** and **2**.^{7,8} As shown in Figure 8B, the pharmacokinetic properties of compound **12** were

significantly improved relative to the previously published values for compounds **1** and **2**.^{7,8} Collectively, these findings demonstrate that introduction of the chiral linker plus replacement of the thiazole ring propyl substituent by a methyl group yields a dCK inhibitor with improved metabolic stability.

CONCLUSION

Structural and inhibition studies of the compounds discussed here, performed using both the purified recombinant enzyme and a cell-based assay, revealed and rationalized the essential determinants for binding to dCK and also guided the type and placement of substituents. This informed the development of the initial leads, compounds **1** and **2**. These compounds contain a propyl group at the 5-position of the thiazole ring, since, as shown earlier, the propyl substituent provides improved affinity for dCK compared to compounds with a methyl group at that position. Unfortunately, this affinity-strengthening propyl group compromised the metabolic stability relative to compounds containing a methyl group at that position. This forced us to revert to the weaker-binding, but more metabolically stable, scaffold of a methyl group at the thiazole ring. With the goal of improving metabolic stability, we tested a chiral methylene methyl sulfur linker between the thiazole and pyrimidine moieties. This linker was found to confer two positive effects: (1) in terms of affinity for dCK, the modified linker compensated for the lack of the thiazole propyl group, and (2) the compounds exhibited improved metabolic stability. The interaction of dCK with compounds containing this linker is specific to the *R*-isomer. This was proven by the dCK-inhibitor crystal structure and by comparing the binding affinities of the *R* versus *S* enantiomers. The new lead compound **12R** is a promising dCK inhibitor, which by perturbing the dNTP pools and inducing DNA replication stress overload could be used in combination with other drugs to specifically trigger synthetic lethality in cancer cells.

EXPERIMENTAL SECTION

Materials. General laboratory reagents were purchased from Fisher (Pittsburgh, PA, USA) and Sigma-Aldrich (St. Louis, MO, USA). Nucleotides were obtained from Sigma. All inhibitors were synthesized at UCLA. Chiral Technologies Inc. (800 North Five Points Road, West Chester, PA 19380, USA) performed the separation of *R* and *S* enantiomers.

Chemistry. General Procedures. Unless otherwise noted, reactions were carried out in oven-dried glassware under an atmosphere of nitrogen using commercially available anhydrous solvents. Solvents used for extractions and chromatography were not anhydrous. 4,6-Diamino-2-mercaptopyrimidine was obtained from drying the hydrate over dynamic vacuum at 110 °C for 20 h. All other reagents obtained from commercial suppliers were reagent grade and used without further purification unless specified. Reactions and chromatography fractions were analyzed by thin-layer chromatography (TLC) using Merck precoated silica gel 60 F₂₅₄ glass plates (250 μm). Visualization was carried out with ultraviolet light, vanillin stain, permanganate stain, or *p*-anisaldehyde stain. Flash column chromatography was performed using E. Merck silica gel 60 (230–400 mesh) with compressed air. ¹H and ¹³C NMR spectra were recorded on a ARX500 (500 MHz), Avance 500 (500 MHz), or Avance 300 (300 MHz) spectrometers. Chemical shifts are reported in parts per million (ppm, δ) using the residual solvent peak as the reference. The coupling constants, *J*, are reported in hertz (Hz), and the resonance patterns are reported with notations as the following: br (broad), s (singlet), d (doublet), t (triplet), q (quartet), and m (multiplet). Electrospray mass spectrometry data were collected with a Waters LCT Premier XE time-of-flight instrument controlled by MassLynx 4.1 software. Samples were dissolved in methanol and

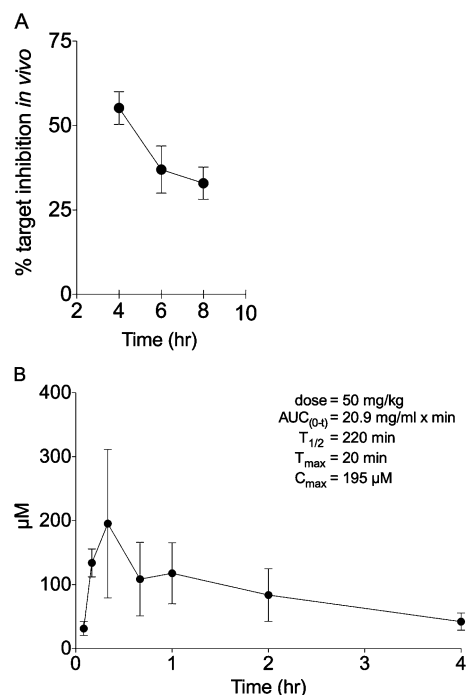


Figure 8. In vivo evaluation of compound **12**. (A) Quantification of PET probe, ¹⁸F-L-FAC, uptake in the liver of C57Bl/6 female mice treated with compound **12** (25 mg/kg) via intraperitoneal injection. Dose formulation: 50% PEG/Tris, pH 7.4. Data are mean values ± SEM for at least *n* = 5 mice/time point. (B) Plasma pharmacokinetic profile of compound **12**. C57Bl/6 female mice were dosed via intraperitoneal injection with 50 mg/kg compound **12** formulated in 50% PEG/Tris, pH 7.4. Data are mean values ± SEM for *n* = 4 mice/time point.

infused using direct loop injection from a Waters Acquity UPLC into the multimode ionization source. The purity of all final compounds was determined to be >95%. Analytical HPLC analysis was performed on a Knauer Smartline HPLC system with a Phenomenex reverse-phase Luna column (5 μ m, 4.6 mm \times 250 mm) with inline Knauer UV (254 nm) detector. Mobile phase: A, 0.1% TFA in H₂O; B, 0.1% TFA in MeCN. Eluent gradient is specified for each described compound. Percent enantiomeric excess (% ee) values were determined via chiral HPLC with a CHIRALPAK IA-3/IA polysaccharide-based immobilized type column (3 μ m, 4.6 mm \times 150 mm) with inline Knauer UV (310 nm) detector. Mobile phase: A, 0.1% TFA in hexanes; B, 0.1% TFA in propanol. Eluent gradient: 50% phase A and 50% phase B. Chromatograms were collected by a GinaStar (Raytest USA, Inc.; Wilmington, NC, USA) analog to digital converter and GinaStar software (Raytest USA, Inc.).

Scheme 1. 3-Ethoxy-4-hydroxybenzothioamide (B). To a mixture of 3-ethoxy-4-hydroxybenzonitrile **A** (2.50 g, 15.3 mmol) in pyridine (35 mL) and triethylamine (2.5 mL) was added ammonium sulfide solution (20 wt % in H₂O, 15.65 mL, 46.0 mmol). The mixture was stirred for 18 h at 60 °C. The reaction mixture was cooled and concentrated in vacuo to remove residual solvent. The resulting residue was washed with brine and extracted with ethyl acetate. The organic layer was dried over anhydrous Na₂SO₄, concentrated in vacuo, and purified by flash column chromatography over silica gel (3:1 ethyl acetate/hexanes) to yield **B** (2.56 g, 13.0 mmol, 85%) as a yellow solid. ¹H NMR (300 MHz, CDCl₃) δ 7.68 (d, *J* = 2.1 Hz, 1H), 7.48 (br s, 1H), 7.28 (dd, *J* = 8.5, 2.1 Hz, 1H), 7.11 (br s, 1H), 6.89 (d, *J* = 8.5 Hz, 1H), 6.03 (s, 1H), 4.21 (q, *J* = 6.9 Hz, 2H), 1.47 (t, *J* = 6.9 Hz, 3H); ¹³C NMR (125 MHz, acetone-*d*₆) δ 200.5, 150.3, 145.8, 131.0, 121.0, 114.0, 112.6, 64.3, 14.1.

1-(2-(3-Ethoxy-4-hydroxyphenyl)-5-methylthiazol-4-yl)-ethan-1-one (C). A mixture of thioamide **B** (1.50 g, 7.6 mmol) and 4-bromopentane-2,3-dione (2.04 g, 11.4 mmol) in ethanol (40 mL) was stirred under refluxing conditions for 4 h. The resulting mixture was cooled and concentrated in vacuo to remove residual solvent. The crude residue was purified by flash column chromatography over silica gel (10:3 hexanes/ethyl acetate) to yield the desired thiazole intermediate **C** (2.00 g, 7.2 mmol, 95%) as a white solid. ¹H NMR (300 MHz, CDCl₃) δ 7.47 (d, *J* = 1.8 Hz, 1H), 7.35 (dd, *J* = 8.2, 1.8 Hz, 1H), 6.96 (d, *J* = 8.1 Hz, 1H), 5.93 (s, 1H), 4.23 (q, *J* = 7.2 Hz, 2H), 2.77 (s, 3H), 2.71 (s, 3H), 1.50 (t, *J* = 6.9 Hz, 3H); ¹³C NMR (75 MHz, CDCl₃) δ 196.0, 162.8, 148.9, 148.0, 146.3, 142.9, 125.9, 120.5, 114.8, 109.4, 64.9, 29.5, 14.9, 13.6.

1-(2-(3-Ethoxy-4-(2-(2-(2-methoxyethoxy)ethoxy)ethoxy)ethoxy)phenyl)-5-methylthiazol-4-yl)ethan-1-one (D). To a solution of thiazole intermediate **C** (1.66 g, 6.0 mmol) in DMF (35 mL) were added Cs₂CO₃ (3.13 g, 9.6 mmol) and 13-chloro-2,5,8,11-tetraoxatridecane (2.19 g, 12.0 mmol). The mixture was stirred for 18 h at 50 °C. After concentration to remove residual solvent, the resulting residue was washed with brine and extracted with ethyl acetate. The organic layer was washed with water three times, dried over anhydrous Na₂SO₄, and concentrated in vacuo, and the crude residue was purified by flash column chromatography over silica gel (1:1 ethyl acetate/hexanes) to yield desired ketone **D** (2.26 g, 5.3 mmol, 89%) as a white solid. ¹H NMR (500 MHz, CDCl₃) δ 7.48 (d, *J* = 2.0 Hz, 1H), 7.38 (dd, *J* = 8.5, 2.0 Hz, 1H), 6.94 (d, *J* = 8.5 Hz, 1H), 4.24–4.20 (m, 2H), 4.17 (q, *J* = 7.0 Hz, 2H), 3.93–3.89 (m, 2H), 3.79–3.75 (m, 2H), 3.70–3.63 (m, 4H), 3.57–3.53 (m, 2H), 3.37 (s, 3H), 2.77 (s, 3H), 2.71 (s, 3H), 1.47 (t, *J* = 7.0 Hz, 3H); ¹³C NMR (125 MHz, CDCl₃) δ 196.0, 162.5, 150.8, 149.4, 149.0, 143.1, 126.9, 119.8, 114.0, 111.4, 72.1, 71.1, 70.8, 70.7, 69.7, 69.0, 64.9, 59.2, 29.5, 15.0, 13.6.

1-(2-(3-Ethoxy-4-(2-(2-(2-methoxyethoxy)ethoxy)ethoxy)phenyl)-5-methylthiazol-4-yl)ethan-1-ol (E). To a stirred solution of ketone **D** (1.06 g, 2.5 mmol) in CH₂Cl₂ (35 mL) cooled to –78 °C was added slowly diisobutylaluminum hydride (1.0 M in THF, 10 mmol, 10 mL). The mixture was allowed to warm to 23 °C and stirred for 1 h. The mixture was cooled to 0 °C and slowly quenched with a saturated aqueous solution of Rochelle's salt. The cloudy solution was stirred for 1 h at 23 °C until the solution became clear again. The resulting solution was extracted with ethyl acetate, washed with brine, dried over

anhydrous Na₂SO₄, and concentrated in vacuo to give the desired alcohol **E** (978 mg, 2.3 mmol, 92%) as a pale yellow solid. ¹H NMR (500 MHz, CDCl₃) δ 7.44 (d, *J* = 2.0 Hz, 1H), 7.33 (dd, *J* = 8.5, 2.0 Hz, 1H), 6.89 (d, *J* = 8.5 Hz, 1H), 4.91 (q, *J* = 6.5 Hz, 1H), 4.22–4.17 (m, 2H), 4.13 (q, *J* = 7.0 Hz, 2H), 3.91–3.86 (m, 2H), 3.76–3.72 (m, 2H), 3.69–3.61 (m, 4H), 3.55–3.51 (m, 2H), 3.35 (s, 3H), 2.37 (s, 3H), 1.52 (d, *J* = 6.0 Hz, 3H), 1.44 (t, *J* = 7.0 Hz, 3H); ¹³C NMR (125 MHz, CDCl₃) δ 164.3, 155.1, 150.0, 149.0, 127.2, 125.8, 119.3, 113.8, 111.0, 71.8, 70.8, 70.6, 70.4, 69.5, 68.7, 64.6, 64.4, 58.9, 24.0, 14.7, 10.7.

4-(1-Chloroethyl)-2-(3-ethoxy-4-(2-(2-(2-methoxyethoxy)ethoxy)ethoxy)phenyl)-5-methylthiazole (F). To a stirred solution of alcohol **E** (425 mg, 1.0 mmol) in CH₂Cl₂ (8 mL) was added thionyl chloride (0.78 mL, 10.0 mmol) slowly at 0 °C. The mixture was allowed to warm to 23 °C and stirred for 1 h. After concentration in vacuo to remove residual solvent, the resulting crude residue was used directly for next step without any further purification because of the instability of chloride **F**.

2-((1-(2-(3-Ethoxy-4-(2-(2-(2-methoxyethoxy)ethoxy)ethoxy)phenyl)-5-methylthiazol-4-yl)ethyl)thio)pyrimidine-4,6-diamine ((\pm)-9). A mixture of crude chloride **F** from the previous step, 4,6-diamino-2-mercaptopyrimidine (625 mg, 4.0 mmol), and K₂CO₃ (552 mg, 4.0 mmol) in DMF (7 mL) was stirred at 70 °C for 1 h. The solution was cooled, concentrated in vacuo, and purified by flash column chromatography over silica gel (25:1 dichloromethane/methanol) to give the desired product (\pm)-**9** (357 mg, 0.65 mmol, 65% in two steps) as a white solid. ¹H NMR (500 MHz, CDCl₃) δ 7.49 (d, *J* = 2.0 Hz, 1H), 7.35 (dd, *J* = 8.5, 2.0 Hz, 1H), 6.90 (d, *J* = 8.5 Hz, 1H), 5.24 (s, 1H), 5.02 (q, *J* = 7.0 Hz, 1H), 4.58 (s, 4H), 4.22–4.18 (m, 2H), 4.15 (q, *J* = 7.0 Hz, 2H), 3.91–3.87 (m, 2H), 3.78–3.75 (m, 2H), 3.69–3.63 (m, 4H), 3.56–3.53 (m, 2H), 3.37 (s, 3H), 2.50 (s, 3H), 1.81 (d, *J* = 7.0 Hz, 3H), 1.46 (t, *J* = 7.0 Hz, 3H); ¹³C NMR (125 MHz, CDCl₃) δ 170.7, 163.8, 163.2 (2), 153.3, 149.9, 149.1, 127.9, 126.8, 119.4, 114.0, 111.3, 80.6, 71.9, 70.9, 70.7, 70.6, 69.7, 68.9, 64.7, 59.1, 37.7, 22.0, 14.8, 11.6; HRMS-ESI (*m/z*) [*M* + *H*]⁺ calcd for C₂₅H₃₅N₅O₅S₂H, 550.2158; found 550.2169.

Scheme 2. 3-Hydroxy-4-methoxybenzothioamide (B). To a mixture of 3-hydroxy-4-methoxybenzonitrile **A** (3.00 g, 20.11 mmol) in pyridine (30 mL) and triethylamine (3 mL) was added ammonium sulfide solution (20 wt % in H₂O, 20.7 mL, 60.3 mmol). The mixture was stirred for 18 h at 60 °C. The reaction mixture was cooled and concentrated in vacuo to remove residual solvent. The resulting residue was washed with brine and extracted with ethyl acetate. The organic layer was dried over anhydrous Na₂SO₄, concentrated in vacuo, and purified by flash column chromatography over silica gel (3:1 ethyl acetate/hexanes) to yield **B** (3.13 g, 17.1 mmol, 85%) as a yellow solid. ¹H NMR (500 MHz, acetone-*d*₆) δ 8.77 (br s, 1H), 8.65 (br s, 1H), 7.85 (s, 1H), 7.59 (d, *J* = 2.5 Hz, 1H), 7.56 (dd, *J* = 8.5, 2.3 Hz, 1H), 6.94 (d, *J* = 8.5 Hz, 1H), 3.88 (s, 3H); ¹³C NMR (125 MHz, acetone-*d*₆) δ 200.7, 150.5, 145.7, 132.4, 119.5, 114.8, 110.2, 55.5.

1-(2-(3-Hydroxy-4-methoxyphenyl)-5-methylthiazol-4-yl)ethan-1-one (C). A mixture of thioamide **B** (2.75 g, 15.0 mmol) and 4-bromopentane-2,3-dione (4.03 g, 22.5 mmol) in ethanol (70 mL) was stirred under refluxing conditions for 4 h. The resulting mixture was cooled and concentrated in vacuo to remove residual solvent. The crude residue was purified by flash column chromatography over silica gel (10:3 hexanes/ethyl acetate) to yield the desired thiazole intermediate **C** (3.79 g, 14.4 mmol, 96%) as a white solid. ¹H NMR (500 MHz, DMSO-*d*₆) δ 9.53 (br s, 1H), 7.34 (d, *J* = 2.0 Hz, 1H), 7.26 (dd, *J* = 8.5, 2.0 Hz, 1H), 6.98 (d, *J* = 8.5 Hz, 1H), 3.80 (s, 3H), 2.66 (s, 3H), 2.57 (s, 3H); ¹³C NMR (125 MHz, DMSO-*d*₆) δ 195.2, 162.5, 150.1, 148.5, 147.1, 142.7, 125.6, 118.2, 112.9, 112.5, 55.9, 29.4, 13.2.

N-(2-(5-(4-Acetyl-5-methylthiazol-2-yl)-2-methoxyphenoxy)ethyl)methanesulfonamide (D). To a solution of thiazole intermediate **C** (1.58 g, 6.0 mmol) in DMF (35 mL) were added Cs₂CO₃ (3.13 g, 9.6 mmol) and *N*-(2-bromoethyl)methanesulfonamide (2.18 g, 10.8 mmol). The mixture was stirred for 72 h at 50 °C. After concentration to remove residual solvent, the resulting residue was washed with brine and extracted with ethyl acetate. The organic layer was washed with water three times, dried over anhydrous Na₂SO₄, and concentrated in vacuo, and the crude residue was purified by flash

column chromatography over silica gel (3:2 ethyl acetate/hexanes) to yield desired ketone **D** (1.89 g, 4.9 mmol, 82%) as a white solid. ^1H NMR (500 MHz, CDCl_3) δ 8.00 (s, 1H), 7.51 (d, $J = 2.0$ Hz, 1H), 7.46 (dd, $J = 8.5, 2.0$ Hz, 1H), 6.92 (d, $J = 8.5$ Hz, 1H), 4.25–4.20 (m, 2H), 3.90 (s, 3H), 3.60–3.55 (m, 2H), 3.03 (s, 3H), 2.76 (s, 3H), 2.70 (s, 3H); ^{13}C NMR (125 MHz, CDCl_3) δ 195.8, 162.5, 151.5, 148.9, 147.8, 143.1, 126.4, 121.1, 112.4, 111.7, 69.1, 55.9, 42.7, 40.6, 29.4, 13.4.

(S)-N-(2-(5-(4-(1-Hydroxyethyl)-5-methylthiazol-2-yl)-2-methoxyphenoxy)ethyl)methanesulfonamide (E). To a stirred solution of (R)-(+)-2-methyl-CBS-oxazaborolidine (6.7 mL of a 1.0 M solution in toluene, 6.7 mmol) in THF (26 mL) at -78°C under Ar was added borane–tetrahydrofuran complex (4.4 mL of a 1.0 M solution in THF, 4.4 mmol) followed by a solution of **D** (284 mg, 0.74 mmol) in THF (14 mL). After addition of the **D** solution with syringe pump for 6 h, the reaction mixture was stirred for another 20 min at -78°C . H_2O (10 mL) and MeOH (5 mL) were added, and the mixture was allowed to warm to room temperature. After concentration to remove residual solvent, the resulting residue was washed with brine and extracted with ethyl acetate. The organic layer was washed with water three times, dried over anhydrous Na_2SO_4 , and concentrated in vacuo, and the crude residue was purified by flash column chromatography twice over silica gel with 3:2 ethyl acetate/hexanes and 40:1 dichloromethane/methanol as washing system separately to yield alcohol **E** (221 mg, 0.57 mmol, 77%, 96% ee) as a white solid. ^1H NMR (500 MHz, acetone- d_6) δ 7.57 (d, $J = 2.0$ Hz, 1H), 7.46 (dd, $J = 8.5, 2.0$ Hz, 1H), 7.05 (d, $J = 8.5$ Hz, 1H), 6.26 (br s, 1H), 5.02–4.95 (m, 1H), 4.21 (t, $J = 5.5$ Hz, 2H), 3.88 (s, 3H), 3.57 (dt, $J = 5.5, 5.5$ Hz, 2H), 3.04 (s, 3H), 2.48 (s, 3H), 1.50 (d, $J = 6.0$ Hz, 3H); ^{13}C NMR (125 MHz, acetone- d_6) δ 162.9, 156.1, 151.3, 148.4, 127.1, 126.8, 119.7, 112.1, 111.4, 68.6, 64.1, 55.3, 42.6, 39.6, 23.0, 10.0.

(S)-1-(2-(4-Methoxy-3-(2-(methylsulfonamido)ethoxy)phenyl)-5-methylthiazol-4-yl)ethyl 2,2,2-Trifluoroacetate (F). To a stirred solution of alcohol **E** (221 mg, 0.57 mmol) in CH_2Cl_2 (13 mL) was added trifluoroacetic anhydride (0.66 mL, 2.9 mmol) slowly at 0°C . After being stirred at 0°C for 30 min, the mixture was allowed to warm to 23°C and stirred for another 30 min. After concentration in vacuo to remove residual solvent, the resulting crude residue was used directly for next step without any further purification because of the instability of the desired trifluoroacetate **F**.

(R)-N-(2-(5-(4-(1-((4,6-Diaminopyrimidin-2-yl)thio)ethyl)-5-methylthiazol-2-yl)-2-methoxyphenoxy)ethyl)methanesulfonamide (10R) and (S)-N-(2-(5-(4-(1-((4,6-Diaminopyrimidin-2-yl)thio)ethyl)-5-methylthiazol-2-yl)-2-methoxyphenoxy)ethyl)methanesulfonamide (12S). A mixture of crude chloride **F** from the previous step and 4,6-diamino-2-mercaptopyrimidine (112 mg, 0.86 mmol) in DMF (5 mL) was stirred at 80°C for 1 h. The solution was cooled, concentrated in vacuo, and purified by flash column chromatography over silica gel (25:1 dichloromethane/methanol) to give the couple of enantiomers **12R** and **12S** (178 mg, 0.35 mmol, 40% ee of **12R**, 61% total yield in two steps) as a white solid. Recrystallization of the enantiomers with MeOH/acetone solvent system gave the **12R** with >93% ee. ^1H NMR (500 MHz, acetone- d_6) δ 7.55 (d, $J = 2.0$ Hz, 1H), 7.48 (dd, $J = 8.5, 2.0$ Hz, 1H), 7.06 (d, $J = 8.5$ Hz, 1H), 6.26 (br s, 1H), 5.60–5.55 (m, 4H), 5.37 (s, 1H), 5.30 (q, $J = 7.0$ Hz, 1H), 4.23 (t, $J = 5.5$ Hz, 2H), 3.89 (s, 3H), 3.58 (dt, $J = 5.5, 5.5$ Hz, 2H), 3.05 (s, 3H), 2.52 (s, 3H), 1.74 (d, $J = 7.0$ Hz, 3H); ^{13}C NMR (125 MHz, DMSO- d_6) δ 168.0, 163.5 (2), 162.9, 153.6, 150.6, 147.8, 126.6, 126.2, 119.5, 112.3, 110.4, 79.0, 67.9, 55.7, 41.9, 36.1, 30.7, 22.2, 11.2; HRMS-ESI (m/z) [$\text{M} + \text{H}$] $^+$ calcd for $\text{C}_{20}\text{H}_{26}\text{N}_6\text{O}_4\text{S}_3\text{H}$, 511.1256; found 511.1259; **12R** [α] $^{19}_\text{D}$ +340.0 (c 0.12, acetone) (93% ee).

Protein Expression and Purification. Protein expression and purification were performed exactly as described by us.⁹ In brief, we used the S74E-C4S-dCK variant, which is the human dCK protein where four solvent-exposed cysteines are mutated into serines (C4S). We showed that the C4S mutant generates better quality crystals without altering the three-dimensional conformation of the enzyme or its enzymatic activity.²² Additionally, the enzyme contained the mutation of Ser74 to glutamic acid (S74E); this mutation serves to mimic the phosphorylated state of this residue. When we refer to dCK in this report, we mean the C4S-S74E-dCK variant. dCK was expressed in

Escherichia coli BL21 C41(DE3) cells using a pET-14b vector; the cells were grown in 2xYT medium and induced with 0.1 mM IPTG for 4 h at 310 K. The cells were harvested, and the pellet was lysed by sonication. The lysate was cleared by centrifugation at 30 000 rev/min for 1 h at 277 K, and the supernatant was loaded onto a 5 mL HisTrap nickel-affinity column (GE Healthcare). The column was washed with 300 mL of a buffer composed of 25 mM Tris-HCl, pH 7.5, 500 mM NaCl, 30 mM imidazole. The bound protein was eluted with the same buffer but containing 250 mM imidazole and was further purified by gel filtration using an S-200 column in a buffer consisting of 25 mM HEPES, pH 7.5, 200 mM sodium citrate, 2 mM EDTA, 3 mM DTT. The protein fractions were pooled, concentrated, aliquoted, flash-frozen in liquid nitrogen, and stored at 193 K until use.

Kinetic Assay. The phosphorylation activity of dCK was determined using a spectroscopic NADH-dependent enzyme-coupled assay.^{2,23} All measurements were taken in triplicate at 310 K in a buffer consisting of 100 mM Tris, pH 7.5, 200 mM KCl, 5 mM MgCl_2 , 0.5 mM EDTA, 0.8 mM phosphoenolpyruvate, 0.4 mM NADH with 50 nM dCK, and 1 mM ATP. $\text{IC}_{50}^{\text{APP}}$ and K_i^{APP} were determined as described by us,⁹ and all data were fitted using the KaleidaGraph software.

IC_{50} Determinations. These were performed in CCRF-CEM acute lymphoblastic leukemia cells as previously described.^{8,9}

PET Studies. PET studies to determine % inhibition of dCK activity in vivo were performed as previously described.^{8,9}

Human Microsomal stability Assays. These assays were performed by Cyprotex (Watertown, MA) according to standard operating protocols.

Plasma Pharmacokinetics of Compounds 10 and 12 in Mice.

These measurements were performed as previously described.^{8,9} Briefly, C57Bl/6 female mice were treated with the dCK inhibitors via intraperitoneal injection. The drugs were administered in 50% polyethylene glycol (PEG 400)/50 mM Tris-HCl, pH 7.5. Five minutes after drug injection, whole blood ($\sim 75\ \mu\text{L}$) was obtained at various time points from the retro-orbital sinus using hematocrit capillary tubes. Samples were centrifuged at 20 000g for 5 min, and the supernatant (5 μL) was transferred into a clean tube. Calibration standards were prepared by spiking various amounts of **11** and **12** in 5 μL of supernatant from the plasma of untreated mice to obtain final concentrations between 0.001 to 100 pmol/ μL . Samples and the calibration standards were mixed with 500 μL ice-cold acetonitrile/water (50/50, v/v) containing an internal standard (**1**). All of the samples were evaporated to dryness in a vacuum centrifuge. The residue was reconstituted in 100 μL of acetonitrile/water (50/50, v/v). Samples (5 μL) were injected onto a reverse phase column (Agilent ZORBAX rapid resolution high definition Eclipse Plus C18, 2.1 mm \times 50 mm, 1.8 μm) equilibrated in water acetonitrile/formic acid, 95/5/0.1, and eluted (200 $\mu\text{L}/\text{min}$) with an increasing concentration of solvent B (acetonitrile/formic acid 100/0.1, v/v: min/% acetonitrile; 0/5, 2/5, 8/80, 9/80, 10/5, 12/5). The effluent from the column was directed to an electrospray ion source (Agilent Jet Stream) connected to a triple quadrupole mass spectrometer (Agilent 6460 QQQ) operating in the positive ion MRM mode. The ion transitions for **1**, **11**, and **12** are 476.2–334.5, 550.2–408.2, and 511.1–369.1 respectively. The peak areas for **11** and **12** were normalized to the peak area of the internal standard, and the plasma concentrations were computed using the standard curves generated by calibration standards spiked in plasma from untreated mice. Approximated values of the area under the curve (AUC), half-life ($T_{1/2}$), maximum concentration in the plasma (C_{max}), and time to reach the maximum concentration (T_{max}) were calculated using Boomer/Multi-Forte PK functions from Microsoft Excel.^{24,25}

Crystallization, X-ray Data Collection, and Refinement.

Crystals of human dCK in complex with inhibitors and UDP were grown at 285 K using the hanging-drop vapor-diffusion method. All dCK-inhibitor complexes were prepared as follows: 1 μL of dCK protein at 10–17 mg/mL in complex with a 2.5-fold molar excess of inhibitor, and 2 mM UDP and 5 mM MgCl_2 were mixed with 1 μL of reservoir buffer solution. The reservoir solution consisted of 0.9–1.5 M trisodium citrate dehydrate and 25 mM HEPES, pH 7.5. Prior to data collection, crystals were soaked in mineral oil for cryoprotection. Diffraction data for dCK in complex with compounds 4–8 were collected on the Life

Sciences Collaborative Access Team (LS-CAT) beamline 21-ID-G. Data for all other complexes (compounds **9–12**) were collected using the in-house X-ray source (Rigaku RU-200 rotating anode) with a RAXIS IV++ image plate detector. Data were processed and scaled with XDS and XSCALE.²⁶ Structures were determined by molecular replacement with MOLREP²⁷ using the dCK structure (PDB entry 4JLN⁹) as a search model. Refinement was conducted using REFMAC,²⁸ and model building was conducted using Coot.²⁹ All inhibitor coordinates and library descriptions were generated using the PRODRG server.³⁰ All data sets were perfectly twinned, and iterative refinements were carried out using REFMAC with the Twin option active. Data collection and refinement statistics are listed in Table 1. Structural figures were prepared using the PyMOL Molecular Graphics System (version 1.6.0, Schrödinger).

Modeling. The *S*-isomer in position 1 and the *R*-isomer in position 2 were generated by flipping the chirality of the linker carbon using Maestro, version 9.1, Schrödinger, LLC, 2010. This program was also used to generate the torsion scans around the bond connecting the chiral linker carbon and the thiazole ring (torsion angle defined by CAC–CBC–CBB–NAO).

Equilibration simulations were performed using the MCPRO 2.0 software package³¹ with the OPLS-AA¹⁷ force field. The protein was solvated in a 30 Å cap of TIP4P water molecules.¹⁶ The protein backbone and all bond lengths within the protein were held fixed. Angles and torsions within 11 Å of the center of the bound molecule were allowed to vary. All degrees of freedom of the bound molecule were sampled. Equilibration began with 5×10^6 configurations of solvent-only moves, followed by 10×10^6 configurations in which the protein and bound molecule were sampled, with additional solvent sampling at every tenth configuration. Equilibrations were performed using Metropolis Monte Carlo in the NPT ensemble at 1 atm and 25 °C. For the unbound structures, optimizations were performed using OPLS-AA. Implicit solvent was simulated with the generalized Born/surface area (GB/SA) method.^{19,21} Energies were assessed using the PDDG/PM3 method³² in the BOSS software package.³¹

■ ASSOCIATED CONTENT

■ Supporting Information

Synthetic schemes for compounds **9** and **10**; general binding information for **1** to dCK; omit maps for compounds **4–10**; in vitro biological data in CEM cells for compounds **S1–S31**; spectroscopic data for compounds **3, 4, 9, 10, 11R, 11S, and 12S**. This material is available free of charge via the Internet at <http://pubs.acs.org>.

Accession Codes

PDB codes for complexes **4–10** and **12R** are the following: 4Q18 (**4**), 4Q19 (**5**), 4Q1A (**6**), 4Q1B (**7**), 4Q1C (**8**), 4Q1D (**9**), 4Q1E (**10**), and 4Q1F (**12R**).

■ AUTHOR INFORMATION

Corresponding Authors

*C.G.R.: e-mail, CRadu@mednet.ucla.edu; phone, 310-825-1205.

*A.L.: e-mail, lavie@uic.edu; phone, 312-355-5029.

Present Address

#J.N.: Institut des Technologies Avancées en Sciences du Vivant (ITAV), Centre National de la Recherche Scientifique (CNRS) USR 3505, Centre Pierre Potier, 31106 Toulouse, France, and Institut de Pharmacologie et de Biologie Structurale (IPBS), CNRS, 31077 Toulouse, France.

Author Contributions

∞J.N., Z.L., R.M.G., and J.W. contributed equally.

Notes

The authors declare the following competing financial interest(s): C.G.R. is a co-inventor of the 18FAC probes used

in this study. This intellectual property has been patented by the University of California and licensed to Sofie Biosciences, a company that both C.G.R. and the University of California own equity in. In addition, C.G.R., M.E.J., A.L.A., and A.L. are co-inventors of the dCK inhibitors used in this study. This intellectual property has been patented by the University of California and optioned to Triangle Therapeutics Inc., a company that C.G.R. and M.E.J. own equity in. This material is based upon work supported by the National Science Foundation under Equipment Grant CHE-1048804 (A.L.), Developmental Project Award from the In Vivo Cellular and Molecular Imaging Center National Cancer Institute P50 CA86306 Award (C.G.R.), National Cancer Institute Grant SU54 CA119347 (C.G.R.), and National Institutes of Health Grant R01 EB013685 (A.L.).

■ ACKNOWLEDGMENTS

We thank Dr. Nagichettiar Satyamurthy for his expert chemistry advice. We thank Larry Pang and Liu Wei for their assistance with PET/CT imaging studies, Dr. Sam Sadeghi and the Ahmanson Translational Imaging Division Cyclotron crew for producing ¹⁸F-L-FAC, and Dr. Jennifer M. Murphy for her assistance in synthesizing compounds **3** and **4**. We also thank Carolann Gemski for help in editing the manuscript. This work was supported by National Institutes of Health [Grant R01 EB013685 to A.L.] and In Vivo Cellular and Molecular Imaging Centers Award National Institutes of Health [Grant P50 CA86306 to C.G.R.] and the U.S. National Cancer Institute [Grant SU54 CA119347 to C.G.R.]. Use of the Advanced Photon Source, an Office of Science User Facility operated for the U.S. Department of Energy (DOE) Office of Science by Argonne National Laboratory, was supported by the U.S. DOE under Contract DE-AC02-06CH11357. Use of the LS-CAT Sector 21 was supported by the Michigan Economic Development Corporation and the Michigan Technology Tri-Corridor (Grant 08SP1000817).

■ ABBREVIATIONS USED

dCK, deoxycytidine kinase; dNTP, deoxyribonucleotide triphosphate; dC, deoxycytidine; dA, deoxyadenosine; dG, deoxyguanosine; ATP, adenosine triphosphate; UTP, uridine triphosphate; PK, pharmacokinetic; PET, positron emission tomography; ¹⁸F-FDG, 2-¹⁸F-fluoro-2-deoxy-D-glucose; ¹⁸F-L-FAC, ¹⁸F-L-1-(2'-deoxy-2'-fluoroarabinofuranosyl) cytosine; PD, pharmacodynamics; PEG, polyethylene glycol; MPEG, methoxy polyethylene glycol; DIBAL-H, diisobutylaluminum hydride; Rochelle's salt, sodium potassium tartrate; CBS, Corey–Bakshi–Shibata; TFA, trifluoroacetate; DMAP, 4-(*N,N*-dimethylamino)-pyridine

■ REFERENCES

- (1) Eriksson, S.; Munch-Petersen, B.; Johansson, K.; Eklund, H. Structure and function of cellular deoxyribonucleoside kinases. *Cell. Mol. Life Sci.* **2002**, *59*, 1327–1346.
- (2) Sabini, E.; Ort, S.; Monnerjahn, C.; Konrad, M.; Lavie, A. Structure of human dCK suggests strategies to improve anticancer and antiviral therapy. *Nat. Struct. Biol.* **2003**, *10*, 513–519.
- (3) Toy, G.; Austin, W. R.; Liao, H. I.; Cheng, D.; Singh, A.; Campbell, D. O.; Ishikawa, T. O.; Lehmann, L. W.; Satyamurthy, N.; Phelps, M. E.; Herschman, H. R.; Czernin, J.; Witte, O. N.; Radu, C. G. Requirement for deoxycytidine kinase in T and B lymphocyte development. *Proc. Natl. Acad. Sci. U.S.A.* **2010**, *107*, 5551–5556.

- (4) Austin, W. R.; Armijo, A. L.; Campbell, D. O.; Singh, A. S.; Hsieh, T.; Nathanson, D.; Herschman, H. R.; Phelps, M. E.; Witte, O. N.; Czernin, J.; Radu, C. G. Nucleoside salvage pathway kinases regulate hematopoiesis by linking nucleotide metabolism with replication stress. *J. Exp. Med.* **2012**, *209*, 2215–2228.
- (5) Choi, O.; Heathcote, D. A.; Ho, K. K.; Muller, P. J.; Ghani, H.; Lam, E. W.; Ashton-Rickardt, P. G.; Rutschmann, S. A deficiency in nucleoside salvage impairs murine lymphocyte development, homeostasis, and survival. *J. Immunol.* **2012**, *188*, 3920–3927.
- (6) Yang, C.; Lee, M.; Hao, J.; Cui, X.; Guo, X.; Smal, C.; Bontemps, F.; Ma, S.; Liu, X.; Engler, D.; Parker, W. B.; Xu, B. Deoxycytidine kinase regulates the G2/M checkpoint through interaction with cyclin-dependent kinase 1 in response to DNA damage. *Nucleic Acids Res.* **2012**, *40*, 9621–9632.
- (7) Nathanson, D. A.; Armijo, A. L.; Tom, M.; Li, Z.; Dimitrova, E.; Austin, W. R.; Nomme, J.; Campbell, D. O.; Ta, L.; Le, T. M.; Lee, J. T.; Darvish, R.; Gordin, A.; Wei, L.; Liao, H. I.; Wilks, M.; Martin, C.; Sadeghi, S.; Murphy, J. M.; Boulos, N.; Phelps, M. E.; Faull, K. F.; Herschman, H. R.; Jung, M. E.; Czernin, J.; Lavie, A.; Radu, C. G. Co-targeting of convergent nucleotide biosynthetic pathways for leukemia eradication. *J. Exp. Med.* **2014**, *211*, 473–486.
- (8) Murphy, J. M.; Armijo, A. L.; Nomme, J.; Lee, C. H.; Smith, Q. A.; Li, Z.; Campbell, D. O.; Liao, H. I.; Nathanson, D. A.; Austin, W. R.; Lee, J. T.; Darvish, R.; Wei, L.; Wang, J.; Su, Y.; Damoiseaux, R.; Sadeghi, S.; Phelps, M. E.; Herschman, H. R.; Czernin, J.; Alexandrova, A. N.; Jung, M. E.; Lavie, A.; Radu, C. G. Development of new deoxycytidine kinase inhibitors and noninvasive in vivo evaluation using positron emission tomography. *J. Med. Chem.* **2013**, *56*, 6696–6708.
- (9) Nomme, J.; Murphy, J. M.; Su, Y.; Sansone, N. D.; Armijo, A. L.; Olson, S. T.; Radu, C.; Lavie, A. Structural characterization of new deoxycytidine kinase inhibitors rationalizes the affinity-determining moieties of the molecules. *Acta Crystallogr., Sect. D: Biol. Crystallogr.* **2014**, *70*, 68–78.
- (10) Godsey, M. H.; Ort, S.; Sabini, E.; Konrad, M.; Lavie, A. Structural basis for the preference of UTP over ATP in human deoxycytidine kinase: illuminating the role of main-chain reorganization. *Biochemistry* **2006**, *45*, 452–461.
- (11) Sabini, E.; Hazra, S.; Ort, S.; Konrad, M.; Lavie, A. Structural basis for substrate promiscuity of dCK. *J. Mol. Biol.* **2008**, *378*, 607–621.
- (12) Shu, Y. Z.; Johnson, B. M.; Yang, T. J. Role of biotransformation studies in minimizing metabolism-related liabilities in drug discovery. *AAPS J.* **2008**, *10*, 178–192.
- (13) Mikhailovskii, D. I.; Mikhailovskaya, V. N. Rearrangement of acetylenic keto alcohols under Meyer–Schuster reaction conditions. *Izv. Vyssh. Uchebn. Zaved., Khim. Khim. Tekhnol.* **1987**, *30*, 29–31.
- (14) Gudipati, V.; Curran, D. P.; Wilcox, C. S. Solution-phase parallel synthesis with oligoethylene glycol sorting tags. Preparation of all four stereoisomers of the hydroxybutenolide fragment of murisolin and related acetogenins. *J. Org. Chem.* **2006**, *71*, 3599–3607.
- (15) Corey, E. J.; Bakshi, R. K.; Shibata, S. Highly enantioselective borane reduction of ketones catalyzed by chiral oxazaborolidines. Mechanism and synthetic implications. *J. Am. Chem. Soc.* **1987**, *109*, 5551–5553.
- (16) Jorgensen, W. L.; Chandrasekhar, J.; Madura, J. D.; Impey, R. W.; Klein, M. L. Comparison of simple potential functions for simulating liquid water. *J. Chem. Phys.* **1983**, *79*, 926–935.
- (17) Jorgensen, W. L.; Maxwell, D. S.; TiradoRives, J. Development and testing of the OPLS all-atom force field on conformational energetics and properties of organic liquids. *J. Am. Chem. Soc.* **1996**, *118*, 11225–11236.
- (18) Jorgensen, W. L.; Tirado-Rives, J. Molecular modeling of organic and biomolecular systems using BOSS and MCPRO. *J. Comput. Chem.* **2005**, *26*, 1689–1700.
- (19) Jorgensen, W. L.; Ulmschneider, J. P.; Tirado-Rives, J. Free energies of hydration from a generalized Born model and an ALL-atom force field. *J. Phys. Chem. B* **2004**, *108*, 16264–16270.
- (20) Repasky, M. P.; Chandrasekhar, J.; Jorgensen, W. L. PDDG/PM3 and PDDG/MNDO: improved semiempirical methods. *J. Comput. Chem.* **2002**, *23*, 1601–1622.
- (21) Still, W. C.; Tempczyk, A.; Hawley, R. C.; Hendrickson, T. Semianalytical treatment of solvation for molecular mechanics and dynamics. *J. Am. Chem. Soc.* **1990**, *112*, 6127–6129.
- (22) Sabini, E.; Hazra, S.; Konrad, M.; Lavie, A. Nonenantioselectivity property of human deoxycytidine kinase explained by structures of the enzyme in complex with L- and D-nucleosides. *J. Med. Chem.* **2007**, *50*, 3004–3014.
- (23) Agarwal, K. C.; Miech, R. P.; Parks, R. E., Jr. Guanylate kinases from human erythrocytes, hog brain, and rat liver. *Methods Enzymol.* **1978**, *51*, 483–490.
- (24) Bourne, D. W. MULTI-FORTE, a microcomputer program for modelling and simulation of pharmacokinetic data. *Comput. Methods Programs Biomed.* **1986**, *23*, 277–281.
- (25) Bourne, D. W. BOOMER, a simulation and modeling program for pharmacokinetic and pharmacodynamic data analysis. *Comput. Methods Programs Biomed.* **1989**, *29*, 191–195.
- (26) Kabsch, W. Xds. *Acta Crystallogr., Sect. D: Biol. Crystallogr.* **2010**, *66*, 125–132.
- (27) Vagin, A.; Teplyakov, A. Molecular replacement with MOLREP. *Acta Crystallogr., Sect. D: Biol. Crystallogr.* **2010**, *66*, 22–25.
- (28) Murshudov, G. N.; Skubak, P.; Lebedev, A. A.; Pannu, N. S.; Steiner, R. A.; Nicholls, R. A.; Winn, M. D.; Long, F.; Vagin, A. A. REFMAC5 for the refinement of macromolecular crystal structures. *Acta Crystallogr., Sect. D: Biol. Crystallogr.* **2011**, *67*, 355–367.
- (29) Emsley, P.; Lohkamp, B.; Scott, W. G.; Cowtan, K. Features and development of Coot. *Acta Crystallogr., Sect. D: Biol. Crystallogr.* **2010**, *66*, 486–501.
- (30) Schüttelkopf, A. W.; van Aalten, D. M. PRODRG: a tool for high-throughput crystallography of protein–ligand complexes. *Acta Crystallogr., Sect. D: Biol. Crystallogr.* **2004**, *60*, 1355–1363.
- (31) Jorgensen, W. L.; Tirado-Rives, J. Molecular modeling of organic and biomolecular systems using BOSS and MCPRO. *J. Comput. Chem.* **2005**, *26*, 1689–1700.
- (32) Repasky, M. P.; Chandrasekhar, J.; Jorgensen, W. L. Improved semiempirical heats of formation through the use of bond and group equivalents. *J. Comput. Chem.* **2002**, *23*, 498–510.